

# Algorithmic realization of the solution to the sign conflict problem for hanging nodes on hp-hexahedral Nédélec elements

S. Kinnewig<sup>1,2</sup>, T. Wick<sup>1,2</sup>, and S. Beuchler<sup>1,2</sup>

<sup>1</sup>Leibniz University Hannover, Institute of Applied Mathematics, Welfengarten 1, 30167 Hannover, Germany

<sup>2</sup>Cluster of Excellence PhoenixD (Photonics, Optics, and Engineering - Innovation Across Disciplines), Leibniz University Hannover, Germany

## Abstract

While working with Nédélec elements on adaptively refined meshes with hanging nodes, the orientation of the hanging edges and faces must be taken into account. Indeed, for non-orientable meshes, there was no solution and implementation available to date. The problem statement and corresponding algorithms are described in great detail. As a model problem, the time-harmonic Maxwell's equations are adopted because Nédélec elements constitute their natural discretization. The implementation is performed within the finite element library deal.II. The algorithms and implementation are demonstrated through four numerical examples on different uniformly and adaptively refined meshes.

## 1 Introduction

The system of Maxwell's equations [22, 37] are fundamental to many fields of research and have numerous practical applications, from Magnetic Induction Tomography (MIT) in medicine [52], geoelectromagnetic modeling in geophysics [24] to quantum computing [35], and quantum communication [36] in optics. As this work is part of the cluster of excellence PhoenixD<sup>1</sup>, we consider applications from the area of photonics and optics. As the designing process of optical components can be challenging, simulations are necessary for support. This involves the simulation of electromagnetic waves within the components, which is done by solving Maxwell's problem for which Nédélec elements form the natural basis. As we consider the time harmonic indefinite Maxwell's problem in this work, specialized techniques are required to solve these kinds of problems. In the literature, several solution techniques are proposed. There are overlapping domain decomposition, see, e.g. the recent publication [12] and the references therein, and nonoverlapping domain decomposition methods, [13], or  $\mathcal{H}$ -matrices [21] which are designed for the time-harmonic case. Note that the system is highly indefinite. Therefore, it becomes very challenging to develop an efficient solver, [20]. Alternatives in the positive definite case are multigrid techniques, [6], [28], or FETI-DP-like algorithms, [48], [18]. Even with these methods, it remains computationally expensive to solve Maxwell's problems. Therefore adaptive strategies, such as local grid refinement, that can keep computational costs reasonable, while increasing the accuracy are highly desirable. This can be achieved with heuristic error indicators, geometry-oriented refinement, residual-based error control, or goal-oriented error control. With this, adaptive grid refinement is one key component in numerical simulations that enables us to handle more complex problems, for example, multi-scale problems for the simulations of integrated optical components.

Our choice for a suitable programming platform is motivated by modern available FEM libraries that include support for high-order Nédélec elements. Various open-source finite element

---

<sup>1</sup><https://www.phoenixd.uni-hannover.de/en/>

libraries allow the use of Nédélec elements of polynomial degree  $p \geq 2$ . The `Elmer FEM` library [29] can handle unstructured grids with a maximum of  $p = 2$ , while `FreeFEM++` [25] can support a maximum of  $p = 3$ . `NGSolve` [43, 42] utilized the basis functions introduced by Schöberl and Zaglmayr [50] to implement high polynomial functions on unstructured grids. `hp3D` [26] implements the Nédélec functions based on the hierarchical polynomial basis from Demkowicz [15]. Also, the following libraries implement high polynomial Nédélec elements, `Fenics` [44] (unstructured), `MFEM` [3], and `GetDP` [23] (unstructured). And `GetDDM` [47], an extension of `GetDP` that implements optimized Schwarz domain decomposition methods, which is a well-established method for solving ill-posed Maxwell’s problems.

We select `deal.II` [5, 4] as it offers high-polynomial Nédélec basis functions based on Schöberl and Zaglmayr’s basis function sets for the complete De-Rham sequence [50]. Also, `deal.II` is well established with a large user basis and good accessibility thanks to its comprehensive documentation, which are essential for sustainable software development and uses tensor product elements. Additionally, it is designed with adaptive mesh refinement in mind, providing a range of functionalities for the computation of error estimators. Due to the use of quadrilateral and hexahedral elements, the local mesh refinement requires the usage of hanging nodes. As a starting point for our implementation of hanging nodes, we use the work of Ledger and Kynch [32] in two dimensions.

The key objective of this work is to address a long-standing open problem that concerns the design of algorithms and corresponding implementation in three dimensions on non-orientable meshes of the Nédélec basis functions on locally refined grids. As previously mentioned, the authors [32] considered high-polynomial Nédélec basis functions to capture skin effects that appear in the MIT problem. Therefore they described a procedure to overcome the sign conflict on  $hp$ -Nédélec elements. In `deal.II`, prior work already utilized hanging nodes for Nédélec elements, for example, the work of Bürg [14]. But there, the old implementation `FE_Nedelec` was used, which can only be applied to oriented grids.

In this work, we extend the class `FE_NedelecSZ`, which can also be applied to non-orientable grids. The extension to three dimensions is non-trivial, as we shall see, and particularly an open problem in `deal.II`. The main work here relies upon the high number of possible configurations we have to cope with. To overcome the sign conflict in the case of hanging edges and faces, we need to adapt the associated constraint matrix that restricts the additional Degrees of Freedom (DoFs) introduced by the hanging edges and faces accordingly. In the three-dimensional case, we have to consider hanging faces. One face has  $2^3$  possible orientations and is refined into four child faces. Consequently, we have to deal with  $2^{15}$  possible configurations. As dealing with every case individually would be even more cumbersome, we perform intelligent grid modifications to reduce the number of cases beforehand significantly. Our goal is to resolve sign conflicts regardless of the polynomial degree involved. To achieve this, we need to comprehend the structure of the constraint matrix so we can develop algorithms that can deal with any given polynomial degree. As one of our aims is to make these results accessible, we provide the most crucial steps as pseudo-code. These accomplishments are exemplarily applied to the time-harmonic Maxwell’s equations, which are solved for four different configurations. Therein, our primary purpose is to show that our algorithms work and our implementation is correct. This is demonstrated through qualitative comparisons and some quantitative results in terms of a computational error analysis.

The outline of this work is as follows. To start our discussion, we will describe the basic operators and polynomials required for the Nédélec basis. Then, we will introduce the  $\mathbf{H}_{\text{curl}}$  conforming basis functions for both two-dimensional and three-dimensional cases, i.e., the Nédélec elements. In section 3, we explain the sign conflict that arises for the Nédélec elements in detail and explain how to overcome the sign conflict, along with some pseudo-code examples. In section 4, we start with the motivation for using non-uniform grids and present the sign conflict that arises in the context of non-uniform grids for Nédélec elements. We also provide a detailed explanation of how to overcome this sign conflict, with some examples of pseudo-code. Section 5 discusses the time-harmonic Maxwell’s equations. Section 6 showcases our implementation by

presenting the numerical results of some benchmark problems.

## 2 $\mathbf{H}_{\text{curl}}$ -conforming element space

We start our problem discussion by comprehensively describing the underlying mathematical spaces to describe the sign conflict. For the discretization of  $\mathbf{H}_{\text{curl}}$ , one must ensure tangential continuity. The De-Rham cohomology (see figure 2.1) [37] tells us that the space with the corresponding properties is the Nédélec space, [38, 39], which is introduced in the following. Our discussion begins with the introduction of the fundamental operators. After that, we make a definition by case, one for the two-dimensional Nédélec elements and one for the three-dimensional Nédélec elements. We like to point the reader to [15, 37] for more details.

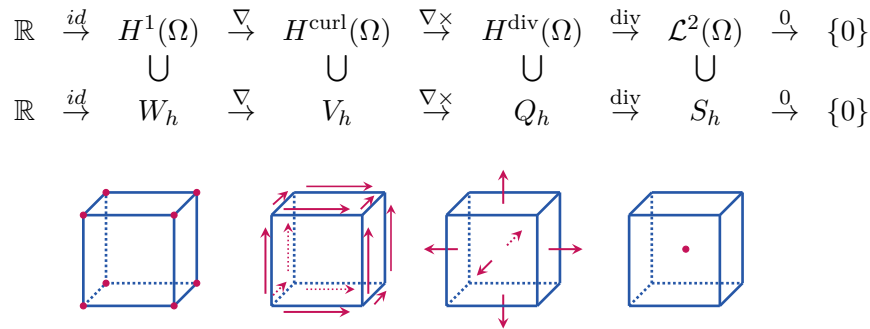


Figure 2.1: The De-Rham complex and its geometric interpretation.

### 2.1 Fundamental operators

For a comprehensive description of the mathematical spaces, we start our discussion by introducing the necessary operators to describe  $\mathbf{H}_{\text{curl}}$ . Therefore, let us assume a scalar  $\psi : \mathbb{R} \rightarrow \mathbb{R}$  and  $\mathbf{a}, \mathbf{b}, \mathbf{c}, \mathbf{v} \in \mathbb{R}^d$ ,  $d \in \{2, 3\}$  to be  $d$ -dimensional vectors. Then the gradient of  $\psi$  is given by  $\nabla \psi = \left( \frac{\partial \psi}{\partial x_1}, \dots, \frac{\partial \psi}{\partial x_d} \right)$ , and the divergence of  $\mathbf{v}$  is given by  $\text{div}(\mathbf{v}) := \nabla \cdot \mathbf{v} := \sum_{i=1}^d \frac{\partial v_i}{\partial x_i}$ . Next,  $\mathbf{a} \cdot \mathbf{b} := \sum_{i=1}^d a_i b_i$  denotes the scalar product. For the description of the cross-product, we need to perform a case analysis, one for the two-dimensional case and one for the three-dimensional case.

$$\begin{array}{l}
 d = 2 : \\
 \left( \begin{array}{c} a_1 \\ a_2 \end{array} \right) \times \left( \begin{array}{c} b_1 \\ b_2 \end{array} \right) = a_1 b_2 - a_2 b_1.
 \end{array}
 \quad \left| \quad \begin{array}{l}
 d = 3 : \\
 \left( \begin{array}{c} a_1 \\ a_2 \\ a_3 \end{array} \right) \times \left( \begin{array}{c} b_1 \\ b_2 \\ b_3 \end{array} \right) = \left( \begin{array}{c} a_2 b_3 - a_3 b_2 \\ a_3 b_1 - a_1 b_3 \\ a_1 b_2 - a_2 b_1 \end{array} \right)
 \end{array} \right. \quad (2.1)$$

with this, we can furthermore write down the description of the curl operator

$$\begin{array}{l}
 d = 2 : \\
 \text{curl}(\mathbf{v}) = \nabla \times \mathbf{v} = \frac{\partial v_2}{\partial x_1} - \frac{\partial b_1}{\partial x_2}
 \end{array}
 \quad \left| \quad \begin{array}{l}
 d = 3 : \\
 \text{curl}(\mathbf{v}) = \nabla \times \mathbf{v} = \left( \begin{array}{c} \frac{\partial v_3}{\partial x_2} - \frac{\partial v_2}{\partial x_3} \\ \frac{\partial v_1}{\partial x_3} - \frac{\partial v_3}{\partial x_1} \\ \frac{\partial v_2}{\partial x_1} - \frac{\partial v_1}{\partial x_2} \end{array} \right).
 \end{array} \right. \quad (2.2)$$

The double cross-product between three vectors is the next operator we need to describe  $\mathbf{H}_{\text{curl}}$  later. The *Graßmann identity* gives the cross-product between these three vectors

$$\mathbf{a} \times (\mathbf{b} \times \mathbf{c}) = (\mathbf{a} \cdot \mathbf{c}) \mathbf{b} - (\mathbf{a} \cdot \mathbf{b}) \mathbf{c}. \quad (2.3)$$

The Graßmann identity is essential for defining the cross-product between three vectors in the two-dimensional case. Based on this definition, we extend the definition of the curl operator to apply to scalar functions in the two-dimensional case

$$\underline{\text{curl}}(\psi) = \left( \begin{array}{c} \frac{\partial \psi}{\partial x_2} \\ -\frac{\partial \psi}{\partial x_1} \end{array} \right). \quad (2.4)$$

## 2.2 Legendre and Integrated Legendre Polynomials

We aim to construct linear independent curl-conforming shape functions with tensor products from one-dimensional orthogonal polynomials. For the polynomial basis, we choose Legendre [46] and integrated Legendre polynomials [45] as they will provide good sparsity in the involved element matrices [50][Chapter 5.2.1]. In the following, we denote the Legendre polynomials by  $l_i(x) = \frac{1}{2^i i!} \frac{d^i}{dx^i} (x^2 - 1)^i \in \mathcal{L}_2(-1, 1)$ , where  $i \in \{0, \dots, p\}$  stands for the polynomial degree. With the following recursive formula, an efficient point evaluation of the Legendre polynomials is possible. For  $x \in [-1, 1]$  let

$$\begin{aligned} l_0(x) &= 1 \\ l_1(x) &= x \\ (n+1)l_{n+1}(x) &= (2n+1)l_n x - n l_{n-1}, \text{ for } n \geq 1. \end{aligned} \tag{2.5}$$

These polynomials span  $P^p([-1, 1])$ , particularly because they fulfill the orthogonality property

$$\int_{-1}^1 l_i(x) l_j(x) dx = \frac{2}{2i+1} \delta_{ij}.$$

From the Legendre polynomials, we can define the integrated Legendre polynomials by  $L_n(x) := \int_{-1}^x l_{n-1}(\xi) d\xi$  for  $x \in [-1, 1]$ . Similar to before, we can define the integrated Legendre polynomials with a recursive formula, which allows for an efficient point evaluation.

$$\begin{aligned} L_1(x) &= x \\ L_2(x) &= \frac{1}{2} (x^2 - 1) \\ (n+1)L_{n+1}(x) &= (2n-1)xL_n(x) - (n-2)L_{n-1}(x), \text{ for } n \geq 2 \end{aligned} \tag{2.6}$$

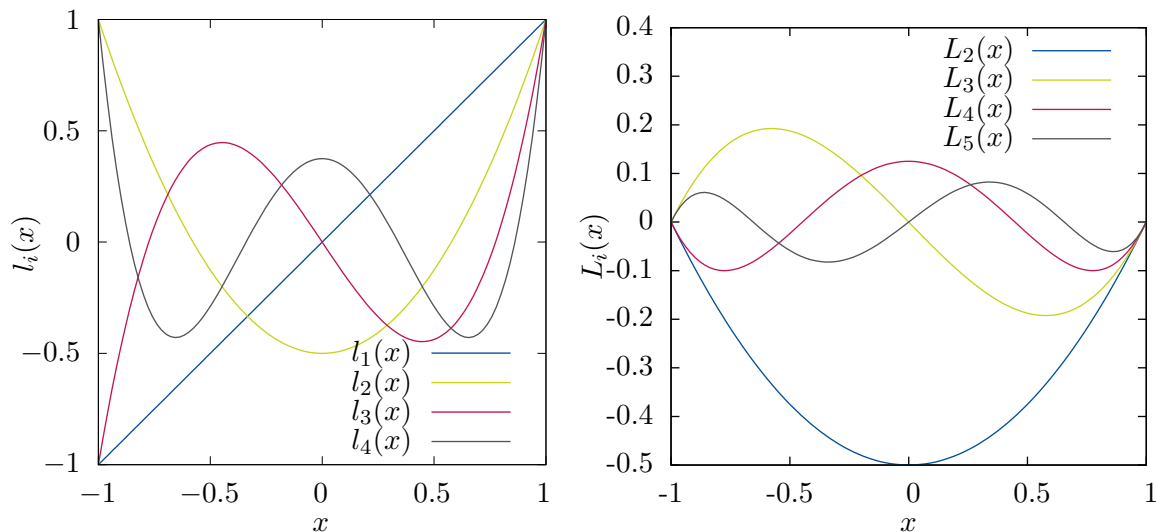


Figure 2.2: Left: Plot of the first four Legendre polynomials. Right: Plot of the first four integrated Legendre polynomials.

For the recursion formula to work, we included  $L_1$  even though  $L_1(x) \neq \int_{-1}^x l_0(\xi) d\xi$ . Above, we have gathered all the necessary tools to construct the Nédélec space. As the curl operator behaves quite differently between the two- and the three-dimensional case, we continue with a definition by cases.

## 2.3 Two-dimensional Nédélec elements

Based on the De-Rham cohomology, we must choose our basis functions out of the Nédélec space  $V_h$ . Therefore, we want to introduce the definition of the space  $V_h$  in the following. The

concept to employ integrated Legendre polynomials as polynomial basis was introduced in [1], for the notation we follow the work of S. Zaglmayr [50, Chapter 5.2]. The enumeration of vertices and edges is based on the implementation in `deal.II` [5]. We define the quadrilateral reference element as  $\mathcal{C}^2 = [0, 1] \times [0, 1]$  with the following parametrization of Figure 2.3.

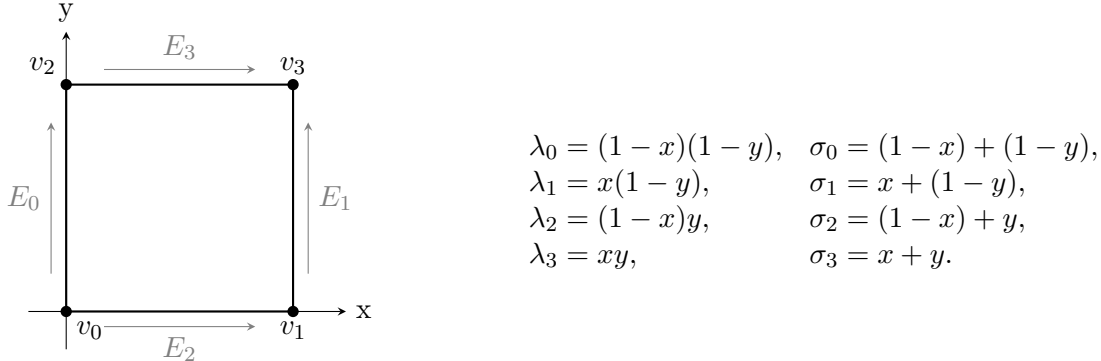


Figure 2.3: Left: Vertex and edge ordering of the two-dimensional reference element. Right: parametrisation of the two-dimensional reference element.

We continue by defining the set of all edges  $\mathcal{E} = \{E_m\}_{0 \leq m < 4}$  with local edge-ordering  $E_m = \{v_i, v_j\}$  where  $(i, j) \in \{(0, 2), (1, 3), (0, 1), (2, 3)\}$ . We denote the cell itself with local vertex-ordering  $C = \{v_0, v_1, v_2, v_3\}$ . The polynomial order is given by  $\mathbf{p} = (\{p_E\}_{E \in \mathcal{E}}, p_C)$ . Based on this, we construct the  $\mathbf{H}_{\text{curl}}$  conforming basis function, where we choose a definition that will provide a good sparsity pattern for the resulting element matrices.

<b><math>\mathbf{H}_{\text{curl}}</math> conforming basis function</b>	
<b>Vertex-based shape functions</b>	
There are no DoFs on the vertices.	
<b>Edge-based shape functions</b>	
for $0 \leq i < p_E$ , $E \in \mathcal{E}$ , where $\lambda_\alpha$ and $\sigma_\alpha$ , $\alpha \in \{0, 1, 2, 3\}$ as defined in figure 2.3	
Lowest order	$\varphi_{E_m}^{N_0} = \frac{1}{2} \nabla (\sigma_{e_2} - \sigma_{e_1}) (\lambda_{e_1} + \lambda_{e_2})$
Higher-order	$\varphi_i^{E_m} = \nabla (L_{i+2} (\sigma_{e_2} - \sigma_{e_1}) (\lambda_{e_1} + \lambda_{e_2}))$
<b>Cell-based functions</b>	
$0 \leq i, j < p_C$ , where $\mathbf{e}_x$ and $\mathbf{e}_y$ are the unit vectors in $x$ - and $y$ -direction correspondingly	
Type 1:	$\varphi_{(i,j)}^{C,1} = \nabla (L_{i+2}(\xi_F) L_{j+2}(\eta_F))$
Type 2:	$\varphi_{(i,j)}^{C,2} = \tilde{\nabla} (L_{i+2}(\xi_F) L_{j+2}(\eta_F))$ where $\tilde{\nabla}(a b) := (a' b - a b')$ is the <i>anti-gradient</i>
Type 3:	$\varphi_{(0,j)}^{C,3} = L_{j+2}(2y - 1) \mathbf{e}_x$ $\varphi_{(i,0)}^{C,3} = L_{i+2}(2x - 1) \mathbf{e}_y$

With the help of the constructed  $\mathbf{H}_{\text{curl}}$  conforming shape functions, we can define a local basis for the two-dimensional Nédélec space on the reference element.

$$V_h(\mathcal{C}^2) := V_h^{N_0}(\mathcal{C}^2) \bigoplus_{E \in \mathcal{E}} V_h^E(\mathcal{C}^2) \oplus V_h^C(\mathcal{C}^2), \quad (2.7)$$

with

$$\begin{aligned}
V_h^{\mathcal{N}_0}(\mathcal{C}^2) &:= \text{span} \left\{ \varphi_E^{\mathcal{N}_0} : E \in \mathcal{E} \right\} \\
V_h^E(\mathcal{C}^2) &:= \text{span} \left\{ \varphi_i^E : 1 \leq i \leq p_E, E \in \mathcal{E} \right\} \\
V_h^C(\mathcal{C}^2) &:= \text{span} \left\{ \varphi_{(i,j)}^{C,t} : 0 \leq i, j < p_C, 1 \leq t \leq 2 \right\} \\
&\quad \oplus \text{span} \left\{ \varphi_{(0,j)}^{C,3} : 0 \leq j < p_C \right\} \oplus \text{span} \left\{ \varphi_{(i,0)}^{C,3} : 0 \leq i < p_C \right\}
\end{aligned}$$

where  $V_h^{\mathcal{N}_0}$  is the space of the *lowest-order Nédélec* function,  $V_h^E$  is the space of the *edge bubbles*, and  $V_h^C$  is the space of the *cell bubbles*. Visualizations of some edge-based basis functions are presented in Figure 3.1. For a discussion that focuses more on the two-dimensional case and provides additional visualizations of the two-dimensional base functions, we refer the reader to [30].

## 2.4 Three-dimensional Nédélec elements

Similar to the previous case, our goal is to construct a basis for the three-dimensional Nédélec space that will lead to a good sparsity pattern of the resulting element matrices. We begin by defining the hexahedral reference element as  $\mathcal{C}^3 = [0, 1] \times [0, 1] \times [0, 1]$ . The enumeration of vertices, edges and faces is based on the implementation in `deal.II` [5]. The parameterization is defined as in Figure 2.4.

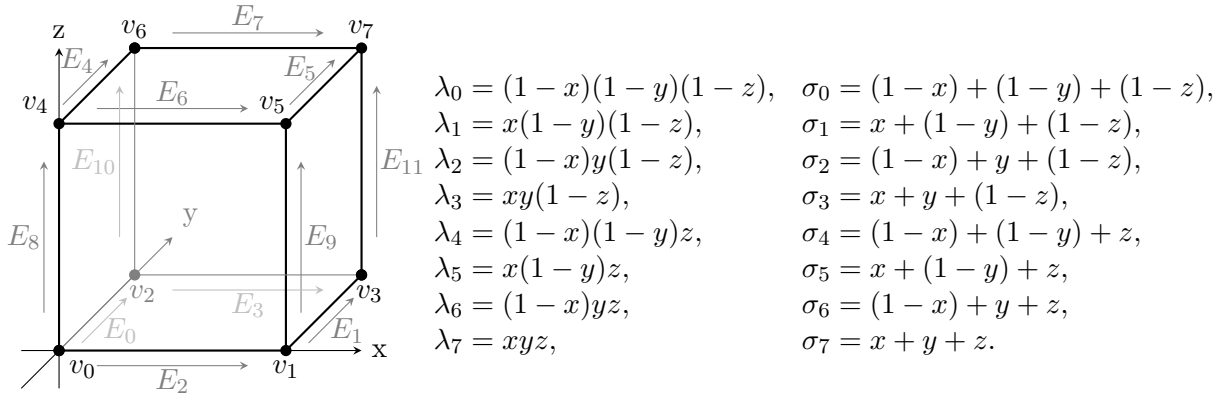


Figure 2.4: Left: Vertex and edge ordering of the three-dimensional reference element. Right: the parametrization of the three-dimensional reference element.

We continue by defining the set of all edges  $\mathcal{E} = \{E_m\}_{0 \leq m < 12}$  with local edge-ordering  $E_m = \{v_i, v_j\}$  as shown in figure 2.4. The local face order is given by

$$\mathcal{F} = \{F_m\}_{0 \leq m < 6} = \left\{ \begin{aligned} &\{v_0, v_2, v_4, v_6\}, \{v_1, v_3, v_5, v_7\}, \{v_0, v_1, v_4, v_5\}, \\ &\{v_2, v_3, v_6, v_7\}, \{v_0, v_1, v_2, v_3\}, \{v_4, v_5, v_6, v_7\} \end{aligned} \right\}. \quad (2.8)$$

A more detailed description of the cell is given in the documentation of `deal.II`<sup>2</sup>. The polynomial order is given by  $\mathbf{p} = (\{p_E\}_{E \in \mathcal{E}}, \{p_F\}_{F \in \mathcal{F}}, p_C)$ .

<sup>2</sup><https://www.dealii.org/current/doxygen/deal.II/structGeometryInfo.html>

<b>H<sub>curl</sub> conforming basis function</b>	
<b>Vertex-based shape functions</b>	
There are no DoFs on the vertices.	
<b>Edge-based shape functions</b>	
for $0 \leq i < p_E$ , $E \in \mathcal{E}$ , where $\lambda_\alpha$ and $\sigma_\alpha$ , $\alpha \in \{0, \dots, 7\}$ as defined in figure 2.4	
Lowest order:	$\varphi_E^{\mathcal{N}_0} = \frac{1}{2} \nabla(\sigma_{e_1} - \sigma_{e_2})(\lambda_{e_1} + \lambda_{e_2})$
Higher order:	$\varphi_i^E = \nabla(L_{i+2}(\sigma_{e_1} - \sigma_{e_2})(\lambda_{e_1} + \lambda_{e_2}))$
<b>Face-based</b>	
For $0 \leq i, j < p_F$ , $F \in \mathcal{F}$ as defined in equation (2.8)	
we define $\lambda_F := \sum_{\alpha=0}^7 \lambda_{f_\alpha}$ and $(\xi_F, \eta_F) := (\sigma_{f_1} - \sigma_{f_2}, \sigma_{f_1} - \sigma_{f_4})$ .	
Type 1:	$\varphi_{(i,j)}^{F_m,1} = \nabla(L_{i+2}(\xi_F)L_{j+2}(\eta_F))$
Type 2:	$\varphi_{(i,j)}^{F_m,2} = \tilde{\nabla}(L_{i+2}(\xi_F)L_{j+2}(\eta_F))$ where $\tilde{\nabla}(a b) := (a' b - a b')$ is the <i>anti-gradient</i>
Type 3:	$\varphi_{(0,j)}^{F_m,3} = L_{j+2}(\eta_F)\lambda_F\nabla\xi_F$ $\varphi_{(i,0)}^{F_m,3} = L_{i+2}(\xi_F)\lambda_F\nabla\eta_F$
<b>Cell-based</b>	
$0 \leq i, j, k < p_C$ , where $\mathbf{e}_x$ , $\mathbf{e}_y$ , $\mathbf{e}_z$ are the basis vectors	
Type 1:	$\varphi_{(i,j,k)}^{C,1} = \nabla(L_{i+2}(2x-1)L_{j+2}(2y-1)L_k(2z-1))$
Type 2:	$\varphi_{(i,j,k)}^{C,2} = \text{diag}(1, -1, 1)\varphi_{(i,j,k)}^{C,1}$ $\varphi_{(i,j,k)}^{C,2} = \text{diag}(1, -1, -1)\varphi_{(i,j,k)}^{C,1}$
Type 3:	$\varphi_{(0,j,k)}^{C,3} = L_{j+2}(2y-1)L_{k+2}(2z-1)\mathbf{e}_x$ $\varphi_{(i,0,k)}^{C,3} = L_{i+2}(2x-1)L_{k+2}(2z-1)\mathbf{e}_y$ $\varphi_{(i,j,0)}^{C,3} = L_{i+2}(2x-1)L_{j+2}(2y-1)\mathbf{e}_z$

With the help of the constructed  $\mathbf{H}_{\text{curl}}$  conforming basis function, we can define a basis for the three-dimensional Nédélec space. The main difference compared to the two-dimensional is that cell bubbles from the two-dimensional case become the face bubbles in the three-dimensional case. Furthermore, we define an additional space for the cell bubbles.

$$V_h(\mathcal{C}^3) := V_h^{\mathcal{N}_0}(\mathcal{C}^3) \oplus \bigoplus_{E \in \mathcal{E}} V_h^E(\mathcal{C}^3) \oplus \bigoplus_{F \in \mathcal{F}} V_h^F(\mathcal{C}^3) \oplus V_h^C(\mathcal{C}^3), \quad (2.9)$$

with

$$\begin{aligned} V_h^{\mathcal{N}_0}(\mathcal{C}^3) &:= \text{span} \left\{ \varphi_E^{\mathcal{N}_0} : E \in \mathcal{E} \right\} \\ V_h^E(\mathcal{C}^3) &:= \text{span} \left\{ \varphi_i^E : 0 \leq i \leq p_E, E \in \mathcal{E} \right\} \\ V_h^F(\mathcal{C}^3) &:= \text{span} \left\{ \varphi_{(i,j)}^{F,t} : 0 \leq i, j \leq p_F, 1 \leq t \leq 2, F \in \mathcal{F} \right\} \\ &\quad \oplus \text{span} \left\{ \varphi_{(0,j)}^{F,3} : 0 \leq j \leq p_F, F \in \mathcal{F} \right\} \oplus \text{span} \left\{ \varphi_{(i,0)}^{F,3} : 0 \leq i \leq p_F, F \in \mathcal{F} \right\} \\ V_h^C(\mathcal{C}^3) &:= \text{span} \left\{ \varphi_{(i,j,k)}^{C,t} : 0 \leq i, j, k \leq p_C, 1 \leq t \leq 2 \right\} \oplus \text{span} \left\{ \varphi_{(0,j,k)}^{C,3} : 0 \leq j, k \leq p_C \oplus \right\} \\ &\quad \oplus \text{span} \left\{ \varphi_{(i,0,k)}^{C,3} : 0 \leq i, k \leq p_C \right\} \oplus \text{span} \left\{ \varphi_{(i,j,0)}^{C,3} : 0 \leq i, j \leq p_C \right\} \end{aligned}$$

where  $V_h^{\mathcal{N}_0}$  is the space of the *lowest-order Nédélec* function,  $V_h^E$  is the space of the *edge bubbles*,  $V_h^F$  is the space of the *face bubbles* and  $V_h^C$  is the space of the *cell bubbles*. Visualizations of some edge-based basis functions are presented in Figure 3.1, and visualization of some face-based basis functions is presented in Figure 3.2.

## 2.5 $\mathbf{H}_{\text{curl}}$ -conforming transformation

In order to extend our definition from the reference element to the physical element, we introduce a  $\mathbf{H}_{\text{curl}}$ -conforming transformation that maps the vectorial shape functions from the reference element  $\mathcal{C}^d$ ,  $d \in \{2, 3\}$  onto the physical element  $C^d$ . The transformation has to preserve the degrees of freedom to be  $\mathbf{H}_{\text{curl}}$ -conform. The transformation also has to map gradient fields from the reference element onto gradient fields on the physical element. In [37, Chapter 3.9, Lemma 3.57, 3.58], the Piola transformation is presented that satisfies these properties. Let us summarize this transformation shortly.

Let  $\Phi_C : \mathcal{C}^d \rightarrow C^d$  be a continuously differentiable, invertible and surjective map,  $\hat{\mathbf{u}} \in \mathbf{H}_{\text{curl}}(\mathcal{C}^d)$ . The transformation

$$\mathbf{u} := F_C^{-T} \hat{\mathbf{u}} \circ \Phi_C^{-1}$$

implies  $\mathbf{u} \in \mathbf{H}_{\text{curl}}(C^d)$  with

$$\begin{array}{l|l} d = 2 : & d = 3 : \\ \text{curl}_x \mathbf{u} = J_C^{-1} \text{curl}_{\hat{x}} \hat{\mathbf{u}} \circ \Phi_C^{-1} & \text{curl}_x \mathbf{u} = J_C^{-1} F_C \text{curl}_{\hat{x}} \hat{\mathbf{u}} \circ \Phi_C^{-1}, \end{array} \quad (2.10)$$

with  $J_C = \det F_C$ .

## 3 Principal problem of the sign-conflict

This section aims to construct the elements so that tangential continuity is ensured between elements.

### 3.1 On the continuity requirements

To ensure the continuity between two neighboring elements, the resulting polynomials on the edges in two dimensions and on the edges and the faces in three dimensions must match. In the previous section, we have defined local edge and face parametrizations. The parameterization we have chosen is either symmetric for even polynomial degrees or anti-symmetric for odd polynomial degrees, as visualized in Figure 3.1.

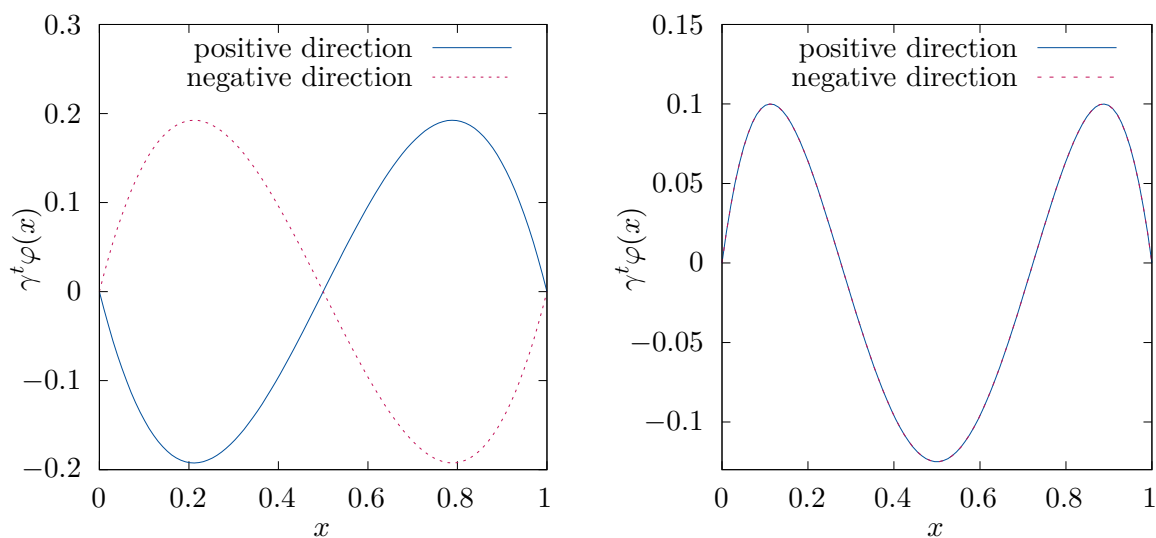


Figure 3.1: On the left-hand side, the anti-symmetric edge function of type 1 with a polynomial degree  $p = 3$ . On the right hand-side, the symmetric edge function of type 1 with a polynomial degree  $p = 4$ .



To ensure that the polynomials between neighboring edges match, we need to ensure that the direction also matches. If the directions do not match, this results in the sign conflict as some polynomials are anti-symmetric see Figure 3.2. This problem does not arise for Lagrange-type elements, as, in that case, the degree of freedom belongs to point evaluations.

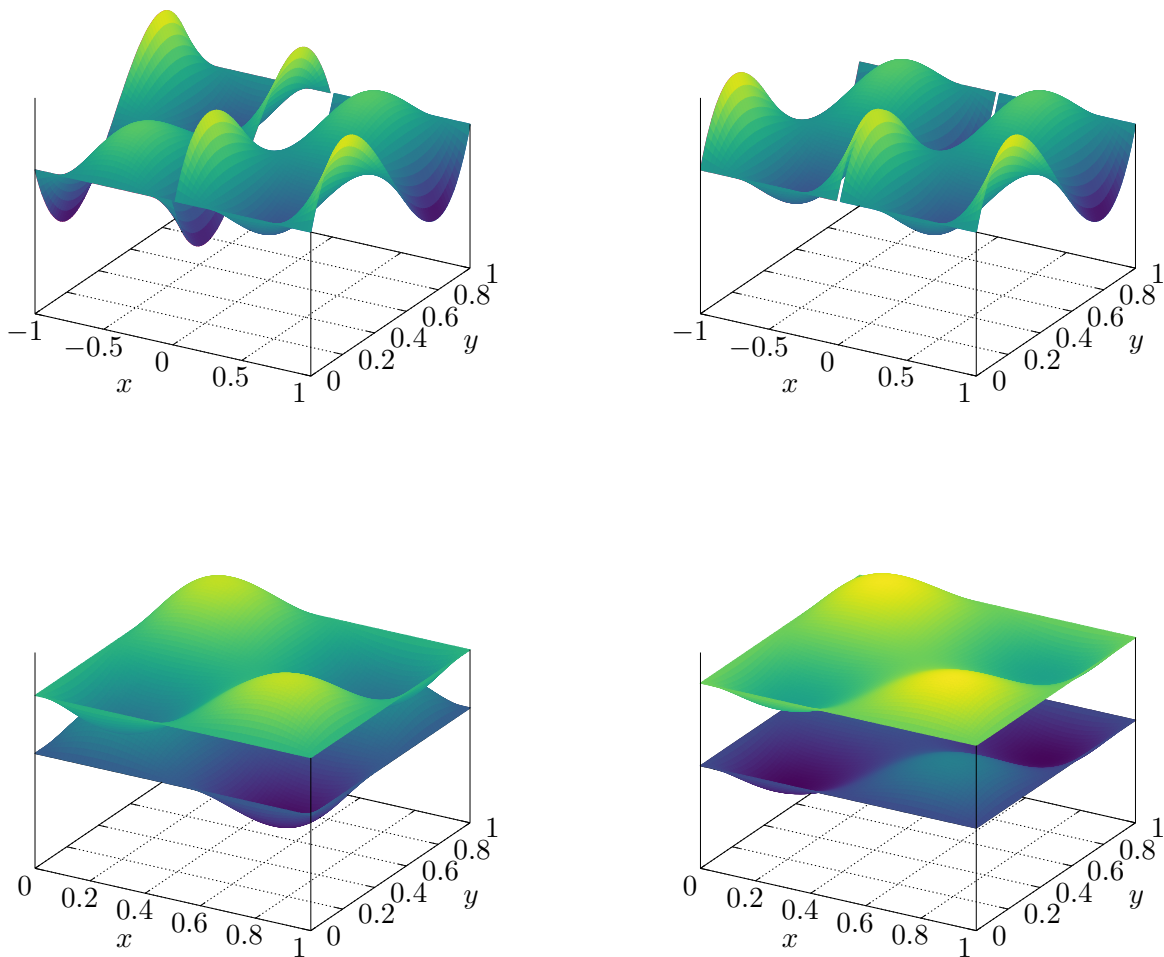


Figure 3.2: Visualization of sign matches and sign conflicts in two and three dimensions with a polynomial degree  $p = 3$ . Top left: Sign-conflict in two dimensions. Top right: Sign-match in two dimensions. Bottom left: Sign-conflict in three dimensions. Bottom right: Sign-match in three dimensions.

### 3.2 Solutions and algorithms for treating the sign conflict

The apparent solution for the sign conflict is to choose a particular direction for each edge and each face. For example, one could define each edge to point from left to right or correspondingly from bottom to top, but it is easy to find a counter-example where this approach will fail, and one will encounter the sign conflict. Therefore we consider the Algorithm 1 and 2, which were proposed by Zaglmayr and Schöberl [50] and implemented into `deal.II` by Kynch and Ledger [32]. Algorithm 1 is applicable for the two-dimensional case and computes a globally consistent orientation for all edges based on the global numeration of dofs. Algorithm 2 computes a globally consistent orientation for all faces based on the global numeration of dofs.

---

**Algorithm 1:**

Compute the global continuous edge orientation  $\tilde{\mathcal{E}} = \{\tilde{E}_0, \dots, \tilde{E}_m\}$  for cell  $\mathcal{K}$  based on the global vertex enumeration.

---

```
1 if dim = 2 then
2   | m = 4;
3 else if dim = 3 then
4   | m = 12;
   // Loop over all edges on cell K
5 for i = 0; i < m do
   // Get the global vertex index of the vertex v0 on edge Ei
6   v0_glob = vertex_index(v0(Ei));
   // Get the global vertex index of the vertex v1 on edge Ei
7   v1_glob = vertex_index(v1(Ei));
   // Redefine E based on the global vertex indices
8   if v0_glob > v1_glob then
9     |  $\tilde{E}_i = [v_1, v_0]$ ;
10  else
11  |  $\tilde{E}_i = [v_0, v_1]$ ;
```

---

**Algorithm 2:**

Compute the global continuous face orientation  $\tilde{\mathcal{F}} = \{\tilde{F}_0, \dots, \tilde{F}_5\}$  for cell  $\mathcal{K}$  based on the global vertex enumeration.

---

```
// Local face vertex order: 2----3
//                          | Fi |
//                          0----1
// Opposite vertex indices for each face
1 vertex_opposite_on_face[4] = {3, 2, 1, 0};
// Adjacent vertex indices for each face
2 vertex_adjacent_on_face[4][2] = {{1, 2}, {0, 3}, {3, 0}, {1, 2}};
// Loop over all faces on cell K
3 for i = 0 to 5 do
   // Get the vertex index with the largest value on the current face
4   f0 = argmax(vertex_index(v_alpha(Fi)));
      alpha in {0, ..., 3}
   // Determine the opposite vertex to the vertex with the largest value
5   f2 = vertex_index(vertex_opposite_on_face[f0]);
   // Determine the indices of the adjacent vertices to the vertex with
   // the largest value
6   l = vertex_index(vertex_adjacent_on_face[f0][0]);
7   r = vertex_index(vertex_adjacent_on_face[f0][1]);
   // Order the adjacent vertices
8   if l > r then
9     | f1 = l;
10    | f3 = r;
11  else
12    | f1 = r;
13    | f3 = l;
   // Store the face Fi, oriented based on the global vertex indices
14   $\tilde{F}_i = [f_0, f_1, f_2, f_3]$ ;
```

---

## 4 Sign Conflict on non-uniform grids

### 4.1 Motivation for the extension to non-uniform grids

In the finite element method context, adaptive grid refinement has proven to be a powerful technique as it allows an adjustment of the resolution of the computational mesh in different simulation regions. The goal is to archive a good balance between accuracy and computational cost by focusing on the more complex parts of the simulation by using local grid refinement in these areas. To decide which parts of the simulation need to be refined can be done either user-defined or automated. For example, automatic, i.e., adaptive, selection can be performed via an error estimator based on the solution's local behavior. The discussion of error estimators is outside the scope of this work, but we refer the reader to [7, 51, 49, 2, 8, 41, 19].

When an element is locally refined in an unstructured mesh, the neighbor elements will be refined to eliminate hanging nodes. This approach is unsuitable for structured meshes since a single local refinement would lead to a uniform global refinement. Therefore, when a structured mesh is locally refined, hanging nodes, edges, and faces in the three-dimensional case are introduced. This leads to a mismatch between the refined and coarse element's number of dofs.

### 4.2 Overview of the implementation of hanging-nodes

Additional constraints must be implemented to overcome the mismatch between refined and coarse elements. These constraints are necessary to ensure that the resulting linear system can be solved numerically. In the case of Nédélec elements, the constraints for non-conforming meshes require that the tangential components of the basis function on the hanging edges and faces match those of the corresponding basis functions on the neighboring unrefined element. Constraints containing weights can be developed by considering a reference setting where we match the tangential constraints. These constraints can be applied to more general shapes with the help of an affine coordinate transformation [16]. The computation of the weights is not in the scope of the work. We refer the reader to [9, 31, 17] for the computation of the weights. The implementation presented here was created using `deal.II` as a programming platform that provides the functionality to compute the weights numerically. Therefore, we focus on modifying the given weights to match the grid's orientation, described in section 4.4.

The hanging edge and face constraints depend on the refined element's orientation and its unrefined neighbor's orientation. Therefore the constraints have to be computed during the runtime. In the previous implementation of the Nédélec elements in `deal.II`<sup>3</sup>, this problem was overcome by assuming pre-assigned edge and face parameterizations, allowing for pre-computed constraints.

---

<sup>3</sup>[https://www.dealii.org/current/doxygen/deal.II/classFE\\_\\_Nedelec.html](https://www.dealii.org/current/doxygen/deal.II/classFE__Nedelec.html)

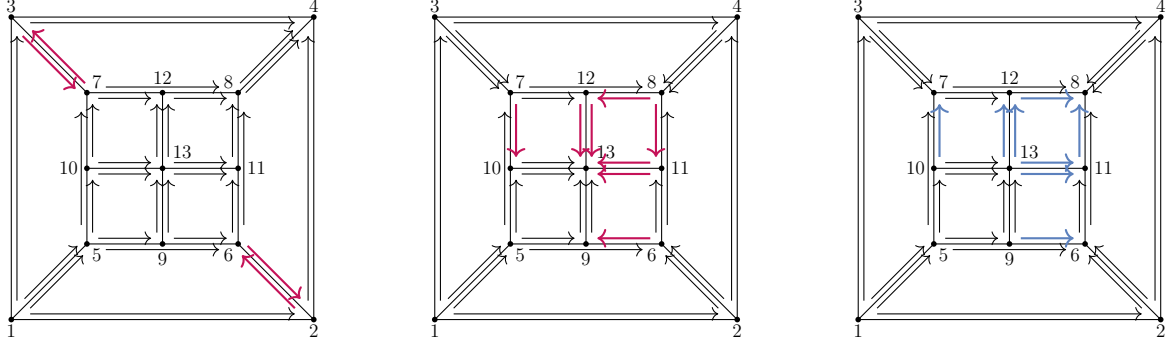


Figure 4.1: Comparison of the resulting orientation of edges from the different implementations of the Nédélec elements in `deal.II` [5]. Edges that result in a sign conflict are marked in red. Left: `FE_Nedelec`, old existing implementation. Centre: Existing implementation of `FE_NedelecSZ` [32], based on [50]. Right: Extension of `FE_NedelecSZ` presented in section 3.

### 4.3 Preparation of the mesh

To greatly simplify the computation of the constraints during the runtime, we extend Algorithm 1 and Algorithm 2 so that the exterior edges and faces match those of the parent’s neighbors.

#### 4.3.1 Preparation of the mesh for the two-dimensional case

---

##### Algorithm 3:

Modification of Algorithm 1, such that global continuity is ensured in the presence of hanging edges.

---

```

// Number of edges, depending on the dimension
1 if dim = 2 then
2   | m = 4;
3 else if dim = 3 then
4   | m = 12;
// Loop over all edges
5 for i = 0 to m - 1 do
6   | // The function neighbor_is_coarser(i) returns true if the ith
7   |   neighbour of the current cell is coarser than the cell itself,
8   |   otherwise it returns false
9   | if neighbor_is_coarser(i) then
10  |   | // Case: hanging edges
11  |   | v0_glob = vertex_index(parent(v0(ei)));
12  |   | v1_glob = vertex_index(parent(v1(ei)));
13  |   | else
14  |   |   | // Case: no hanging edges
15  |   |   | v0_glob = vertex_index(v0(ei));
16  |   |   | v1_glob = vertex_index(v1(ei));
17  |   | // redefine the edge Ei based on the global vertex indices
18  |   | if v0_glob > v1_glob then
19  |   |   |  $\tilde{E}_i = [v_1, v_0]$ ;
20  |   | else
21  |   |   |  $\tilde{E}_i = [v_0, v_1]$ ;

```

---

To gain more insight into the Algorithm 3, we consider Figure 4.2, which compares the direction of the edges of the unrefined parent element with the direction of the edges of the refined child

elements. To visually differentiate between those two, the parent element is depicted in black, while the hanging vertices and edges of the child elements are highlighted in blue. The parent element consists of the two vertices  $v_0$  and  $v_1$  and the edge  $E_0^P$  that points from  $v_0$  to  $v_1$ . The left child element consists of the vertices  $v_0$  and  $v_1$  and the edge  $E_0^C$  between them, and the right child element consists of the vertices  $v_2$  and  $v_1$  and edge  $E_1^C$ .



Figure 4.2: Comparison between the direction of edges between the parent and child elements in `deal.II`. Left: The orientation of the edges of the children where chosen based on the Algorithm 1. Right: The orientation of the edges of the children where chosen such that they match the direction of the parent edges as in the Algorithm 3. Edges whose direction differ from the left image are highlighted in red.

Suppose we apply Algorithm 1 in `deal.II` to a refined element, the edges will always point to the hanging vertex, the hanging vertex as a higher global dof index as the outer vertices. As long as the neighbor element has the same refinement level, the global orientation stays consistent. However, when the neighbor is coarser, one has to apply the Algorithm 3; see Figure 4.3.



Figure 4.3: Comparing the orientation of a grid resulting from Algorithm 1 (left) and Algorithm 3 (right). Differences are highlighted in red.

### 4.3.2 Preparation of the mesh for the three-dimensional case

In Algorithm 3, we have focused on the orientation of hanging edges, which applies to two-dimensional cases. However, we also have to deal with hanging faces in the three-dimensional case. Therefore we introduce the Algorithm 4.

---

**Algorithm 4:**

Modification of Algorithm 2, such that global continuity is ensured in the presence of hanging faces and edges.

---

```
1 vertex_opposite_on_face[4] = {3, 2, 1, 0};
2 vertex_adjacent_on_face[4][2] = {{1, 2}, {0, 3}, {3, 0}, {1, 2}};
  // Loop over all faces on cell  $\mathcal{K}$ 
3 for  $i = 0$  to 5 do
4   if neighbor_is_coarser( $i$ ) then
5     // Case: hanging faces
6      $f_0 = \operatorname{argmax}_{\alpha \in \{0, \dots, 3\}}(\operatorname{vertex\_index}(v_\alpha(\operatorname{parent}(F_i))))$ ;
7      $l = \operatorname{vertex\_index}(\operatorname{parent}(\operatorname{vertex\_adjacent\_on\_face}[f_0][0]))$ ;
8      $r = \operatorname{vertex\_index}(\operatorname{parent}(\operatorname{vertex\_adjacent\_on\_face}[f_0][1]))$ ;
9   else
10    // Case: no hanging faces
11     $f_0 = \operatorname{argmax}_{\alpha \in \{0, \dots, 3\}}(\operatorname{vertex\_index}(v_\alpha(F_i)))$ ;
12     $l = \operatorname{vertex\_index}(\operatorname{vertex\_adjacent\_on\_face}[f_0][0])$ ;
13     $r = \operatorname{vertex\_index}(\operatorname{vertex\_adjacent\_on\_face}[f_0][1])$ ;
14  // Compute the face direction
15   $f_2 = \operatorname{vertex\_index}(\operatorname{vertex\_opposite\_on\_face}[f_0])$ ;
16  if  $l > r$  then
17     $f_1 = l$ ;
18     $f_3 = r$ ;
19  else
20     $f_1 = r$ ;
21     $f_3 = l$ ;
22  // Store the face  $F_i$ , oriented based on the global vertex indices
23   $\tilde{F}_i = [f_0, f_1, f_2, f_3]$ ;
```

---

To gain more insight into the Algorithm 4, we visualize the orientation of the refined face in Figure 4.4. As before, the parent element is depicted in black, and the direction of its children is in blue. In addition, the face direction is indicated here.

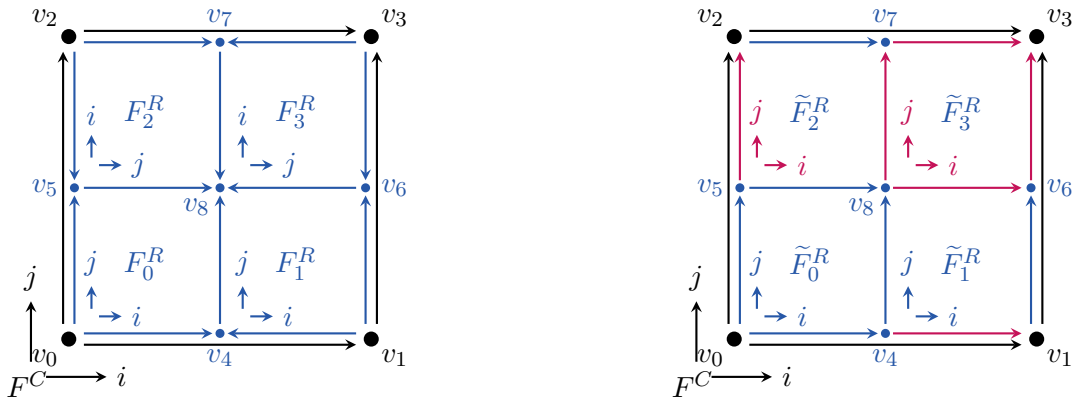


Figure 4.4: Comparison between the direction of edges and faces between the parent and child elements in deal.II. Left: The orientation of the edges and faces of the children were chosen based on Algorithm 1 and 2 correspondingly. Right: The orientation of the edges of the children where chosen such that they match the direction of the parent edges based on Algorithms 3 and 4. Edges and faces that direction differ from the left image are marked in red.

### 4.3.3 Challenging refinement cases

In the three-dimensional case, there are specific configurations where the element has an edge that neighbors a coarser element, even though the neighbors of all faces of that element are of the same refinement level as the element itself. For an example of such a configuration, see Figure 4.5.

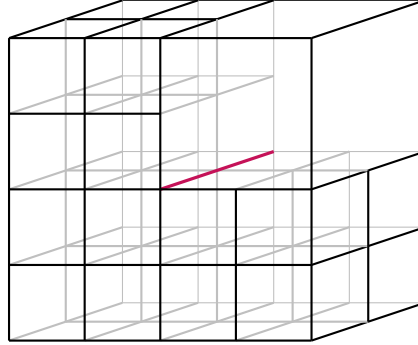


Figure 4.5: The lower left element has only neighbors of the same refinement level, even though one of its edges also has a coarser neighbor; that edge is marked in red.

To greatly simplify the computation of the hanging edges and hanging face constraints later on, we provide Algorithm 5, which deals with these specific configurations.

---

**Algorithm 5:** Check for hanging edges on elements whose face neighbors are the same refinement level.

---

```

// List of neighbors we need to check:
1 neighbor_list = { 2, 2, 4, 4, 0, 0 };
// Loop over all faces
2 for i = 0 to 5 do
3   if not neighbor_is_coarser(i) then
4     if neighbor(i) → neighbor_is_coarser(neighbor_list[i]) then
5       v0_glob = vertex_index(parent(v0(ei)));
6       v1_glob = vertex_index(parent(v1(ei)));
7       if v0_glob > v1_glob then
8         |  $\tilde{E}_i = [v_1, v_0]$ ;
9       else
10      |  $\tilde{E}_i = [v_0, v_1]$ ;
11   if neighbor(i) → neighbor_is_coarser(neighbor_list[i] + 1) then
12     v0_glob = vertex_index(parent(v0(ei)));
13     v1_glob = vertex_index(parent(v1(ei)));
14     if v0_glob > v1_glob then
15       |  $\tilde{E}_i = [v_1, v_0]$ ;
16     else
17       |  $\tilde{E}_i = [v_0, v_1]$ ;

```

---

## 4.4 Modification of the constraint matrix

In the previous section, we introduced several algorithms to prepare the orientation of the grid to make it easier to adapt the hanging node constraints to general grids. Based on that work, we now modify the constraint matrix. Here we like to point out that the considered enumeration of DoFs is based on the ordering of the edges and vertices as in `deal.II`. The basic concept is the

same to extend this work to other FEM software, but one must consider the edges and vertices enumeration of that specific software.

#### 4.4.1 Constraints for hanging edges

The two most prominent approaches to deal with the additional DoFs originating from the hanging edges and faces are the following. First, one can apply suitable projections and use iterative solvers [27]. The second method on which we focus in this work is to impose constraints on the additional DoFs of the refined element by expressing them as a linear combination of the coarse's DoFs in the following way:

$$\varphi_r = [\alpha_{i,j}]_{i,j}^{n,m} \cdot \varphi_c,$$

where  $\varphi_r$  is the vector of the basis function on the refined element,  $\varphi_c$  is the vector of basis functions on the coarse element, and  $\alpha_{i,j}$  are the weights between the corresponding basis functions. Figure 4.6 considers the most simple example. Here one takes into account that the Nédélec functions are edge-based. Therefore we obtain two DoFs on the coarse element and four DoFs on the refinement element.

$$\begin{pmatrix} \varphi_{C_0}^{N_0} \\ \varphi_{C_1}^{N_0} \end{pmatrix} = \begin{pmatrix} 1/2 \\ 1/2 \end{pmatrix} \cdot \begin{pmatrix} \varphi_M^{N_0} \end{pmatrix}$$


Figure 4.6: Left: Linear system to constraint the additional degrees of freedom introduced by a hanging edge in two dimensions, with polynomial degree  $p = 1$ . Right: Visualising the edge corresponding to the linear system on the left-hand side. The colors indicate to which position the degrees of freedom belong.

#### 4.4.2 Resolving the sign conflict on hanging edges

We have just introduced the constraint matrix for oriented meshes so far. To extend the implementation of Nédélec elements in `deal.II`, for working with non-oriented meshes, we need to modify the constraint matrix accordingly to the orientation of the mesh. Therefore we must compare the refined element's vertex order with the coarse neighbor's vertex order, similar to the Algorithm 3. If the vertex order between the refined and coarse neighbors does not match, we must adapt the constraint matrix accordingly. Furthermore, we need to consider to which underlying base function each entry of the constraint matrix belongs. We introduced the base function for the Nédélec elements in detail in section 2. Here we need to consider if the underlying basis function is symmetric or anti-symmetric. Since entries that map an anti-symmetric shape-function to a symmetric shape-function and vice versa are multiplied by  $-1$ . Entries that map from symmetric shape functions to symmetric shape functions do not change. Also, entries that map from anti-symmetric shape functions to anti-symmetric do not change, as both sign changes cancel each other out. This is summarised in the Tabular 4.1.

		coarse element	
		symmetric	anti-symmetric
refined element	symmetric	1	-1
	anti-symmetric	-1	1

Table 4.1: Transformation of the constraint matrix if the vertex order between the refined element and its coarse neighbor does not match based on the symmetry of the underlying shape function.



Given this information, we can formulate the following Algorithm to resolve the sign conflict on hanging edges.

---

**Algorithm 6:**

Adapt the constraint matrix to the orientation of the mesh.

---

```

// Get the orientation of the coarse edge
1 parent_orientation = get_edge_orientation( $E^C$ );
// Loop over all children of  $\mathcal{K}$ 
2 for  $k = 0$  to 1 do
    // Get the orientation of the refined edge
    3 child_orientation = get_edge_orientation( $E_k^R$ );
    // Get the corresponding local sub-constraint matrix
    4 constraint_matrix =  $C_k$ 
    // Loop over all entries of the constraint matrix
    5 for  $i, j$  in constraint_matrix do
        // Check if the shape function is anti-symmetric
        6 if  $(i + j) \% 2 = 1$  then
            // Check if the orientations differ
            7 if child_orientation  $\neq$  parent_orientation then
                // Flip the sign of the entry
                8 constraint_matrix[ $i, j$ ] = -constraint_matrix[ $i, j$ ];
        // Write the modified local sub-constraint matrix into the global
        // constraint matrix
    9 local_constraint_to_global(constraint_matrix)

```

---

Again we want to consider the smallest example possible. Here we have to choose polynomial degree  $p = 2$  for the underlying base function. As for  $p = 1$ , the constraint matrix would not change at all. See Figure 4.7.

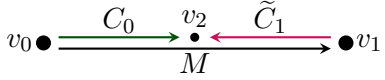
$$\begin{pmatrix} \varphi_{C_0}^{\mathcal{N}_0} \\ \varphi_1^{C_0} \\ \varphi_{C_1}^{\mathcal{N}_0} \\ \varphi_1^{C_1} \end{pmatrix} = \begin{pmatrix} 1/2 & 1/2 \\ 0 & 1/4 \\ 1/2 & -1/2 \\ 0 & 1/4 \end{pmatrix} \cdot \begin{pmatrix} \varphi_M^{\mathcal{N}_0} \\ \varphi_1^M \end{pmatrix}$$


Figure 4.7: The resulting constraint matrix when algorithm 6 is applied to the constraint matrix corresponds to a hanging edge with polynomial degree  $p = 2$ .

#### 4.4.3 Constraints for hanging faces

So far, we have focused solely on the orientation of hanging edges, which applies to two-dimensional cases. For the extension to three dimensions, we need to consider hanging faces. Hanging faces consist of eight external and four internal lines and four faces, as visualized in Figure 4.8. The coarse element consists of four external lines and one face. Therefore the size of the constraint matrix increases accordingly.

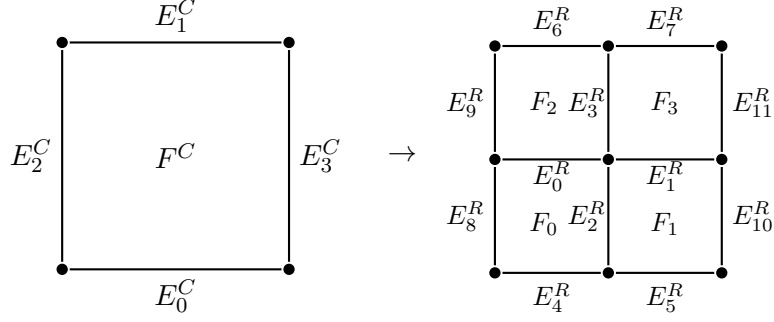


Figure 4.8: Enumeration of edges and faces.

As the constraint matrix increases significantly in size for hanging faces, particularly in the first non-trivial case where the polynomial degree is  $p = 2$ , we only visualize the structure of the constraint matrix in Figure 4.9. It is worth noting that for  $p = 1$ , there are no DoFs on the faces, rendering this case unsuitable for our study on the structure of hanging faces.

$$\begin{pmatrix} l(E_0^R) \\ l(E_1^R) \\ l(E_2^R) \\ l(E_3^R) \\ l(E_4^R) \\ \vdots \\ l(E_7^R) \\ l(E_8^R) \\ \vdots \\ l(E_{11}^R) \\ l(F_0^R) \\ \vdots \\ l(F_3^R) \end{pmatrix} = \begin{pmatrix} C_{(0,0)} & C_{(0,1)} & C_{(0,2)} & C_{(0,3)} & C_{(0,4)} \\ C_{(1,0)} & C_{(1,1)} & C_{(1,2)} & C_{(1,3)} & C_{(1,4)} \\ C_{(2,0)} & C_{(2,1)} & C_{(2,2)} & C_{(2,3)} & C_{(2,4)} \\ C_{(3,0)} & C_{(3,1)} & C_{(3,2)} & C_{(3,3)} & C_{(3,4)} \\ C_{(4,0)} & C_{(4,1)} & 0 & 0 & 0 \\ \vdots & \vdots & \vdots & \vdots & \vdots \\ C_{(7,0)} & C_{(7,1)} & 0 & 0 & 0 \\ 0 & 0 & C_{(8,2)} & C_{(8,3)} & 0 \\ \vdots & \vdots & \vdots & \vdots & \vdots \\ 0 & 0 & C_{(11,2)} & C_{(11,3)} & 0 \\ 0 & 0 & 0 & 0 & C_{(12,4)} \\ \vdots & \vdots & \vdots & \vdots & \vdots \\ 0 & 0 & 0 & 0 & C_{(15,4)} \end{pmatrix} \cdot \begin{pmatrix} r(E_0^C) \\ r(E_1^C) \\ r(E_2^C) \\ r(E_3^C) \\ r(F^C) \end{pmatrix}$$

Figure 4.9: The structure of the constraint matrix. As a simplification, we group the basis function into different groups, where  $l(E_i^R)$ ,  $i \in \{0, 11\}$  denotes the vector of all basis functions corresponding to the edge  $E_i^R$  on the refined element.  $l(F_i^R)$ ,  $i \in \{0, 3\}$  denotes the vector of all basis functions on the face  $F_i^R$ . Analog  $l(E_i^C)$ ,  $i \in \{0, 3\}$  denotes the vector of all basis functions corresponding to the edge  $E_i^C$  on the coarse element.  $l(F_i^R)$ ,  $i \in \{0, 3\}$  denotes the vector of all basis functions on the face  $F_i^R$ .  $C_{(i,j)}$  denotes the corresponding sub-constraint matrix between  $l(E_i^C)$  and  $r(E_j^R)$ .

#### 4.4.4 Resolving the sign conflict on hanging faces

Due to the complexity of the structure of the constraint matrix, we consider the different sub-constraint matrices, i.e., the  $C_{(i,j)}$  in Figure 4.9, independently as this is the natural decomposition of the problem. Thereby we consider each hanging edge and face independently. Based on our prior study of the problem, we can determine which coarse edge and face directions we must consider depending on the current hanging edge or face we want to constrain. This information is also shown in Figure 4.9.

#### Constraints for the outer edges

We begin by adapting the signs of sub-constraint matrices that describe the map edges on the

coarse element to outer edges, i.e., edges  $E_4, \dots, E_{11}$  in Figure 4.8, on the refined element. This is most straightforward as it is analogous to the two-dimensional case discussed in section 4.4.2. Based on the vertex order, we determine the direction of the edges and then adapt the signs of the corresponding entries in the constraint matrix.

### Constraints for the faces

Next, we discuss how to adapt the constraint matrix for that map to the refined faces  $F_0, \dots, F_3$ . For an edge, there are only two possible configurations (pointing from the left to the right or vice versa). However, in the three-dimensional case, we must consider the  $x$ -direction and the  $y$ -direction and which direction is prioritized. This results in  $2^3 = 8$  possible orientations. These are visualized in Figure 4.10. The diagonal arrow denotes whether the  $x$  or the  $y$ -direction is prioritized. If the diagonal arrow points to the upper left vertex, the  $x$ -direction is prioritized. If the diagonal arrow points to the lower right vertex, the  $y$ -direction is prioritized.

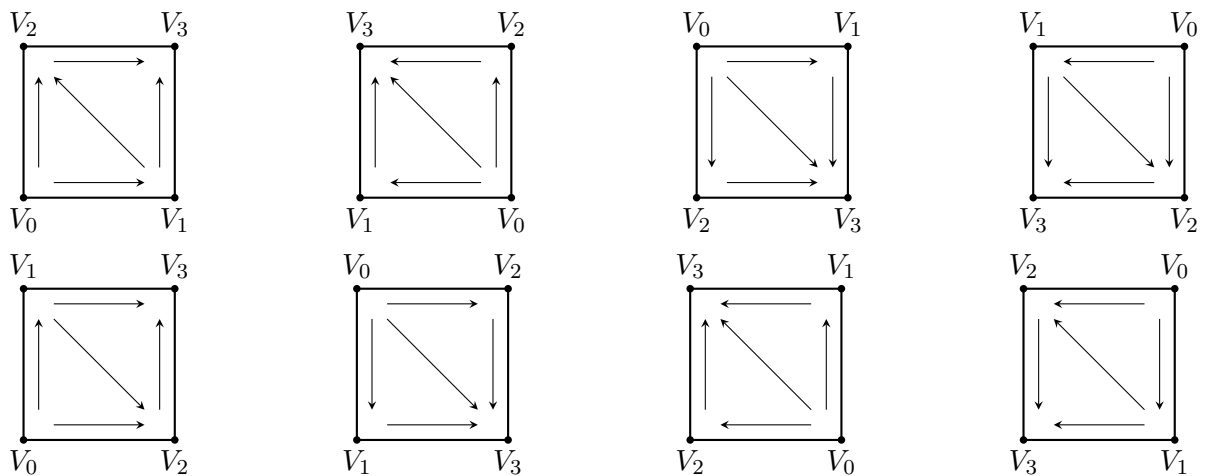
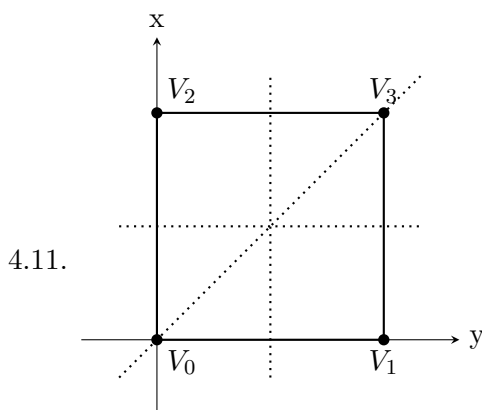


Figure 4.10: Visualization of the  $2^3 = 8$  possible orientations for faces.

We must modify the constraint matrix accordingly based on the given configuration of the coarse and refined faces. We can geometrically interpret the necessary operations as  $x$ -axis inversion,  $y$ -axis inversion, and  $x$ - and  $y$ -axis exchange. These operations are visualized in Figure



4.11.

Figure 4.11: The geometrical interpretation of the different operations must be applied to the sub-constraint matrices.

Begin	x	y	x/y	result
	×			
	×	×		
	×	×	×	

Table 4.2: Look-up table to identify which operations have to be applied to the sub-constraint matrix to map correctly from a particular coarse face to a refined face.

Because of the more complex nature of these operations, we provide them here as high-level

pseudo-code.

In Algorithm 7, we present how to perform an  $x$ -inversion on the constraint matrix for a given cell  $\mathcal{K}$ . The  $y$ -inversion is analogous to the  $x$ -inversion. The Algorithm 8 explains the  $x$ - and  $y$ -axis exchange.

---

**Algorithm 7:** Description of the  $x$ -axis inversion

---

```

// Convert the dobble indices from the faces into one index,  $p$  denotes
// the polynomial degree of the underling base function.
1 face_index ( $i, j$ ):
2   return ( $i \cdot (p - 1) + j$ );
// get the orientation of the coarse cell in x-direction
3 parent_orientation_x = get_orientation_x( $\mathcal{K}$ );
// Loop over all child faces of  $\mathcal{K}$ 
4 for  $k = 0$  to 3 do
    // get the orientation of the refined cell in x-direction
5   child_orientation_x = get_child_orientation_x( $\mathcal{K}, F_k$ );
    // Get the corresponding local sub-constraint matrix
6   constraint_matrix =  $C_{k,4}$ ;
    // loop over the index  $i$ , remark that  $i$  is decomposed into  $ix$  and  $iy$ 
7   for  $ix = 0$  to  $p - 1$  do
8     for  $iy = 0$  to  $p - 1$  do
9       // loop over the index  $j$ , remark that  $j$  is decomposed into  $jx$ 
10      // and  $iy$ 
11      for  $jx = 0$  to  $p - 1$  do
12        for  $jy = 0$  to  $p - 1$  do
13          if is_odd( $ix + jx$ ) then
14            constraint_matrix(face_index( $ix, iy$ ), face_index( $jx, jy$ )) *= -1.0;
    // Write the modified local sub-constraint matrix into the global
    // constraint matrix
13 local_constraint_to_global(constraint_matrix)

```

---

---

**Algorithm 8:** Description of the x- and y-axis exchange

---

```
1 face_index (i, j):
2   return (i · (p − 1)) + j;
   // get the xy-orientation of the coarse cell
3 parent_orientation_xy = get_orientation_xy( $\mathcal{K}$ );
   // Loop over all child faces of  $\mathcal{K}$ 
4 for k = 0 to 3 do
   // get the corresponding orientation
5   child_orientation_xy = get_child_orientation_xy( $\mathcal{K}$ ,  $F_k^R$ );
   // Get the corresponding local sub-constraint matrix
6   constraint_matrix =  $C_{k,4}$ ;
7   constraint_matrix_before =  $C_{k,4}$ ;
   // loop over i
8   for ix = 0 to p − 1 do
9     for iy = 0 to p − 1 do
10      // loop over j
11      for jx = 0 to p − 1 do
12        for jy = 0 to p − 1 do
13          // swap the x and y direction
          constraint_matrix(face_index(ix, iy), face_index(jx, jy)) =
          constraint_matrix_before(face_index (ix, iy), face_index(jy, jx));
13 local_constraint_to_global(constraint_matrix)
```

---

Given a particular configuration of the coarse face, we can now create a look-up table, which of these operations have to be applied to the sub-constraint matrix to map to a particular refined face correctly. For an example of such a look-up table, see Tabular 4.2.

### Constraints for the inner edges

At last, we describe the process of adapting the constraint matrix for the inner edges  $E_0, \dots, E_3$ . We treat this case last, as this configuration is the most complex, requiring extensive modifications of the constraint matrix. As shown in Figure 4.9, the refined interior edges are constrained by all four coarse edges and the coarse face. For the sub-constraint matrices that map from the coarse edges parallel to the refined edge, we are considering. We employ the same approach for the outer edges. Next, we need to apply a similar approach as for the faces, taking into account the direction of the internal edge, which can be either in the  $x$ - or  $y$ -direction. We must apply the corresponding axis inversion as described above according to the orientation of the internal edge we are currently considering. However, we must deal with one additional case for the inner edges: the sub-constraint matrix mapping from the coarse edges orthogonal to the refined internal edge. This works again similarly to the case of the outer edges. The corresponding sub-constraint matrices must also be adapted according to the direction of the coarse edges parallel to the refined edge. This is shown in the Algorithm 9.

---

**Algorithm 9:** Inversion of the direction of the refined internal edge parallel to the  $x$ -axis.

---

```

// Convert the double indices from the faces into one index,  $p$  denotes
// the polynomial degree of the underlying base function.
1 face_index ( $i, j$ ):
2   return ( $i \cdot (p - 1) + j$ );
// get the orientation of the coarse cell in x-direction
3 parent_orientation_x = get_orientation_x( $\mathcal{K}$ );
// Loop over all internal edges, parallel to the  $x$ -axis
4 for  $k = 0$  to 1 do
   // get the orientation of the refined cell in x-direction
5   child_orientation_x = get_child_orientation_x( $\mathcal{K}, E_k^R$ );
   // Loop over all the internal edges, parallel to the  $x$ -axis
6   for  $l = 2$  to 3 do
     // Get the corresponding local sub-constraint matrix
7     constraint_matrix =  $C_{k,l}$ ;
     // loop over the index  $i$ 
8     for  $ix = 0$  to  $p - 1$  do
9       for  $iy = 0$  to  $p - 1$  do
10        // loop over the index  $j$ 
11        for  $jx = 0$  to  $p - 1$  do
12          for  $jy = 0$  to  $p - 1$  do
13            if is_odd( $ix + jx$ ) then
14              constraint_matrix(face_index( $ix, iy$ ), face_index( $jx, jy$ )) *=
                -1.0;
   local_constraint_to_global(constraint_matrix)

```

---

## 5 Model problem: time-harmonic Maxwell's equations and numerical solution

Let  $\Omega \subset \mathbb{R}^d$ ,  $d \in \{2, 3\}$  be a bounded modelling domain with sufficiently smooth boundary  $\Gamma = \Gamma^{\text{inc}} \cup \Gamma^\infty$ , where  $\Gamma^\infty$  is an absorbing boundary condition and  $\Gamma^{\text{inc}}$  is the boundary condition for some given incident electric field. Find the electric field  $\mathbf{u} \in \mathbf{H}_{\text{curl}}(\Omega) := \{\mathbf{v} \in \mathcal{L}^2(\Omega), \text{curl}(\mathbf{v}) \in \mathcal{L}^2(\Omega)\}$  such that,

$$\begin{cases} \text{curl}(\mu^{-1} \text{curl}(\mathbf{u})) - \varepsilon \omega^2 \mathbf{u} &= \mathbf{0} & \text{in } \Omega \\ \mu^{-1} \gamma^t(\text{curl}(\mathbf{u})) - i \kappa \omega \gamma^T(\mathbf{u}) &= \mathbf{0} & \text{on } \Gamma^\infty \\ \mu^{-1} \gamma^t(\text{curl}(\mathbf{u})) - i \kappa \omega \gamma^T(\mathbf{u}) &= 2i \omega \gamma^T(\mathbf{u}^{\text{inc}}) & \text{on } \Gamma^{\text{inc}}, \end{cases} \quad (5.1)$$

where  $\mathbf{u}^{\text{inc}} : \mathbb{R}^d \rightarrow \mathbb{C}^d$ ,  $d \in \{2, 3\}$  is some given incident electric field,  $\mu \in \mathbb{R}^+$  is the relative magnetic permeability,  $\kappa = \sqrt{\varepsilon}$ ,  $\varepsilon \in \mathbb{C}$  relative permittivity,  $\omega = \frac{2\pi}{\lambda}$  is the wavenumber and  $\lambda \in \mathbb{R}^+$  is the wavelength. For the traces we define the space of well-defined surface divergence fields

$$\mathbf{H}_{\text{div}}^{-1/2}(\Gamma) := \{\mathbf{v} \in \mathbf{H}^{-1/2}(\Gamma) : \mathbf{v} \cdot \mathbf{n} = 0, \text{div}_\Gamma \mathbf{v} \in \mathbf{H}^{-1/2}(\Gamma)\}$$

and the space of well-defined surface curls

$$\mathbf{H}_{\text{curl}}^{-1/2}(\Gamma) := \{\mathbf{v} \in \mathbf{H}^{-1/2} : \mathbf{v} \cdot \mathbf{n} = 0, \text{curl}_\Gamma \mathbf{v} \in \mathbf{H}^{-1/2}(\Gamma)\},$$

then the traces are given by

$$\begin{aligned}\gamma^t &: \mathbf{H}_{\text{curl}}(\Omega) \rightarrow \mathbf{H}_{\text{div}}^{-1/2}(\Gamma), & \gamma^t(\mathbf{v}) &= \mathbf{n} \times \mathbf{v} & \text{and} \\ \gamma^T &: \mathbf{H}_{\text{curl}}(\Omega) \rightarrow \mathbf{H}_{\text{curl}}^{-1/2}(\Gamma), & \gamma^T(\mathbf{v}) &= \mathbf{n} \times (\mathbf{v} \times \mathbf{n})\end{aligned}$$

where  $\mathbf{n}$  denotes the outward normal to  $\Omega$ . System (5.1) is called time-harmonic, because the time dependence can be expressed by  $e^{i\omega\tau}$ , where  $\tau \geq 0$  denotes the time. For the derivation of the time-harmonic Maxwell's equations we refer the reader to [37].

Before we derive the weak formulation let us recapitulate, that with integration by parts, we can reformulate an integral in the following way

$$\int_{\Omega} \text{curl}(\mathbf{v}) \mathbf{w} \, dx = \int_{\Omega} \mathbf{v} \text{curl}(\mathbf{w}) \, dx + \int_{\partial\Omega} (\mathbf{v} \times \mathbf{w}) \mathbf{w} \, ds. \quad (5.2)$$

Next, we want to derive the weak formulation of equation (5.1).

$$\begin{aligned}\int_{\Omega} \text{curl}(\mu^{-1} \text{curl}(\mathbf{u})) \varphi \, dx - \varepsilon\omega^2 \int_{\Omega} \mathbf{u} \varphi \, dx &= \mathbf{0} \\ \stackrel{(5.2)}{\Rightarrow} \int_{\Omega} \mu^{-1} \text{curl}(\mathbf{E}) \text{curl}(\varphi) \, dx - \varepsilon\omega^2 \int_{\Omega} \mathbf{E} \varphi \, dx + \int_{\partial\Omega} \mu^{-1} \gamma^t(\text{curl}(\mathbf{E})) \varphi \, ds &= \mathbf{0}.\end{aligned}$$

Finally we apply the definition of the boundaries  $\Gamma^{\infty}$  and  $\Gamma^{\text{inc}}$  and obtain the weak form, which is given by: Find  $\mathbf{u} \in \mathbf{H}_{\text{curl}}(\Omega)$  such that for all  $\varphi \in \mathbf{H}_{\text{curl}}(\Omega)$

$$\begin{aligned}\int_{\Omega} (\mu^{-1} \text{curl}(\mathbf{u}) \text{curl}(\varphi) - \varepsilon\omega^2 \mathbf{u} \varphi) \, dx + ik\omega \int_{\Gamma^{\infty}} \gamma^T(\mathbf{u}) \gamma^T(\varphi) \, ds \\ = \int_{\Gamma^{\text{inc}}} \gamma^T(\mathbf{u}^{\text{inc}}) \gamma^T(\varphi) \, ds.\end{aligned} \quad (5.3)$$

Notice that we have chosen the plane wave injection for the incident field [34, Section I.3.2.a]. The numerical solution of the resulting linear system is rather challenging, as it is ill-posed. So specialized methods have to be employed. A well-known approach to address the time-harmonic Maxwell's equation is based on combining direct solvers and domain decomposition methods [13, 10]. Here the basic idea is to divide the problem into small enough sub-problem so that a direct solver can handle each sub-problem. Another approach is to find suitable preconditioners for iterative solvers, for example, with the help of H-matrices. As the computation of such preconditioners is quite challenging, these methods often have to be combined with a domain decomposition method [40].

## 6 Numerical tests

In this section, we present some numerical examples, to demonstrate our implementation of hanging nodes for Nédélec elements especially on non-orientable geometries. Therefore, we consider four examples.

### 6.1 Minimal test case: simple cube

As a first proof of concept, we want to compare the results of the new implementation of hanging nodes for Nédélec elements with the existing implementation of hanging nodes for Nédélec elements. We have to consider that the existing implementation only works for orientable grids. We use a simple cube refined once globally as a minimal test case. So it consists of eight cells. Then, one of these cells is refined adaptively. The resulting grid is orientable. Therefore we can use this test case as a first proof of the concept and compare our results with the existing implementation of hanging nodes in `deal.II`.

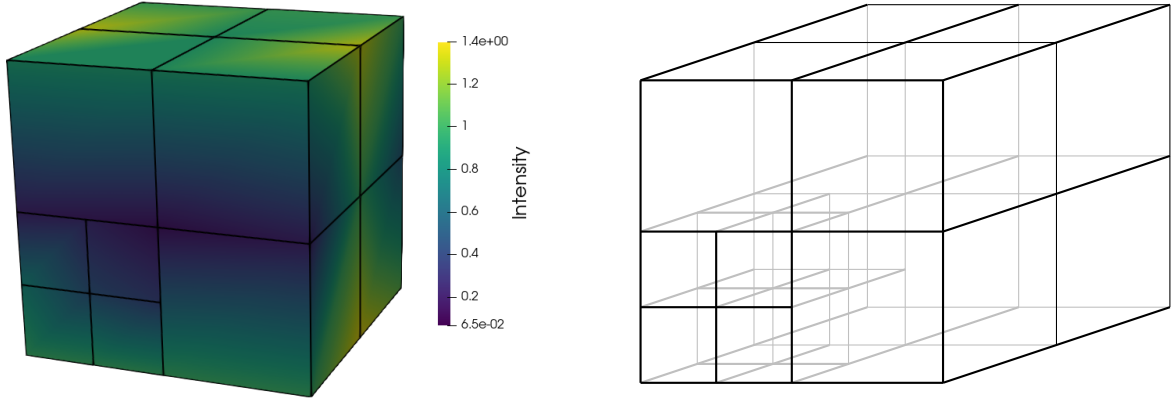


Figure 6.1: Left: The Grid used for the minimal test case. Right: The intensity distribution of the electric field on that grid.

Comparing the results of the existing implementation and our new implementation of hanging nodes for Nédélec elements show no difference. It holds  $|E_{\text{existing}} - E_{\text{new}}|_{\infty} < 1e - 16$ . Therefore, we continue with more complicated applications in the following.

## 6.2 Quantitative computational analysis on a simple cube

To further validate our new implementation of the hanging nodes, we consider different goal functionals on different (adaptive-)refinement levels, where we use the finest level with 2 080 944 DoFs as numerical reference. As a benchmark problem, we consider a cylindrical fiber made from  $\text{SiO}_2$  with a refractive index of  $n_{\text{SiO}_2} = 2.0257$  surrounded by air  $n_{\text{air}} = 1.0000$  and an incident wave with a wavelength of  $\lambda = 375$  nm. We evaluate the following three goal functionals: the point value  $J_P(u) = u(x)$ , the face integral  $J_F(u) = \int_f u(s)ds$ , and the domain integral  $J_D(u) = \int_{\omega} u(x)dx$ . The results are presented in Table 6.1. In this test, we employ the polynomial degree of the underlying base functions high enough so that all features of the base functions are tested. Therefore, we choose a polynomial of degree  $p = 3$ .

Level	DoFs	$ J_P(u_l) - J_P(u_{ref}) $	$ J_F(u_l) - J_F(u_{ref}) $	$ J_D(u_l) - J_D(u_{ref}) $
1	29436	0.052260	0.155929	0.020955
2	146520	0.010761	0.012619	0.000261
3	681432	0.000079	0.001181	0.000084

Table 6.1: Results from evaluating the goal functionals on different levels.

The errors resulting from the sign conflict are visible in the intensity plot. Consequently, we compare in Figure 6.2 the intensity plots resulting from the existing implementation of the Nédélec elements in `deal.II`. The intensity plot is computed in the first column with the `FE_Nedelec`<sup>4</sup> class, which does not support non-oriented meshes. The resulting intensity distribution differs from the correct solution. The results computed with the existing implementation of the `FE_NedelecSZ`<sup>5</sup> class are presented in the second column. Here the solution on the uniform refined grid is correct, but on the isotropic refined grid, the solution differs from the correct solution. The result from the here presented extension of the `FE_NedelecSZ` class is shown in the third column. Here is also the solution on the isotropic refined grid correct.

<sup>4</sup>[https://www.dealii.org/current/doxygen/deal.II/classFE\\_\\_Nedelec.html](https://www.dealii.org/current/doxygen/deal.II/classFE__Nedelec.html)

<sup>5</sup>[https://www.dealii.org/current/doxygen/deal.II/classFE\\_\\_NedelecSZ.html](https://www.dealii.org/current/doxygen/deal.II/classFE__NedelecSZ.html)



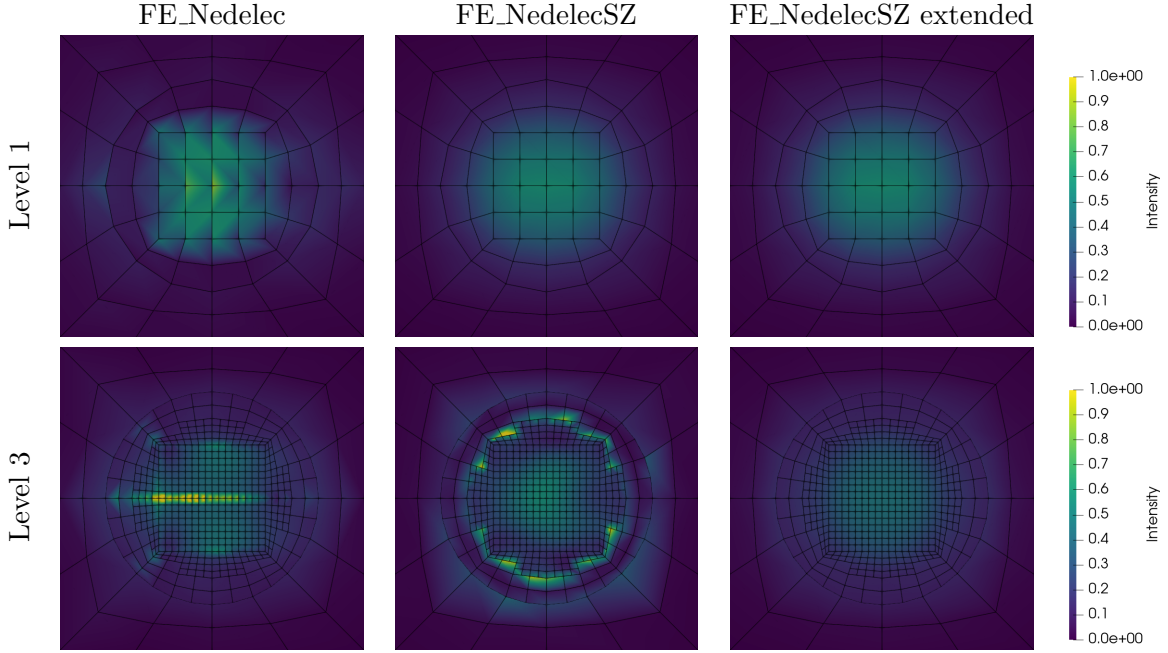


Figure 6.2: Tabular overview of the different implementations from the Nédélec elements on the example of the intensity plot from the fiber presented in section 6.2 for two refinement levels. Only homogenous refinement was applied to the first row, and adaptive mesh refinement introduced hanging edges in the second. FE\_Nedelec, FE\_NedelecSZ, and the here-presented extension of FE\_NedelecSZ were used for the columns.

### 6.3 Silver ball in vacuum

To validate our implementation for non-orientable grids, we compute the scattering of a planar electromagnetic wave on a silver ball in a vacuum once via FEM and once with Mie's theory [11, Chapter 4], a well-established method for calculating the scattering of electromagnetic waves by spherical particles.

For our simulation, we assume a silver ball with a radius of 100nm and a complex refractive index of  $r_{Ag} = 0.0 + 4.0i$  that is hit by an incident planar wave with a wavelength of  $\lambda = 500$  nm and linear polarisation in the  $x$ -direction. To compute the scattering of the electric field in three dimensions via FEM, we use Nédélec elements with polynomial order  $p = 2$  as basis functions and solve the time-harmonic Maxwell's equations, as presented in chapter 5. Also, we employ a domain decomposition of the computational grid by decomposing the grid into four concentric shells. Each shell is further divided into two half-shells, resulting in eight subdomains. Here, using hanging nodes allows us to use adaptive mesh refinement around the silver ball, where the electric field is expected to vary significantly. Thereby we can increase the accuracy of our simulation without adding too many additional DoFs. For the computation of the electric field via Mie's theory, we employed the library `scattnlay` [33].

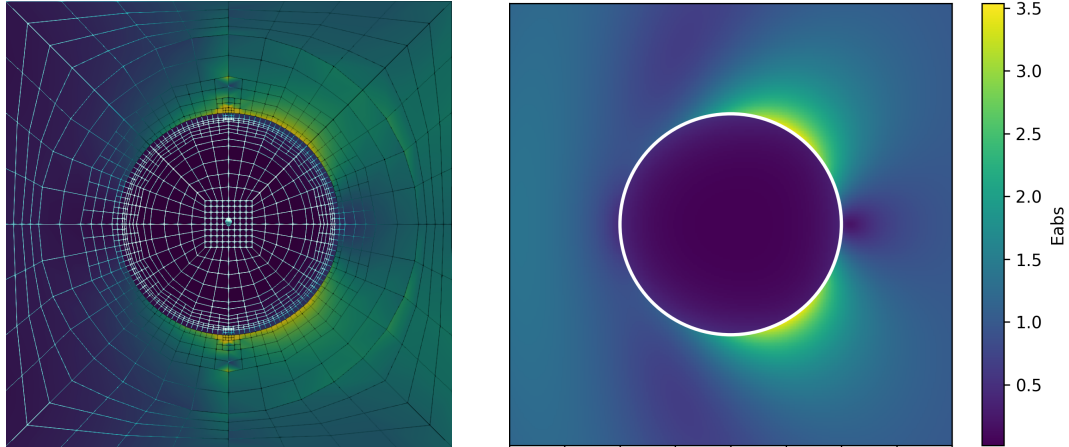


Figure 6.3: The x-y cross-section of the intensity of an electric field scattered from a silver ball in a vacuum. Left: The solution computed via FEM. Right: The solution computed with scattnlay.

In Figure 6.3, we are comparing the result obtained by Mie’s theory, and once obtained with FEM, we obtain a generally good agreement between the results. However, the computation of the scattered electric field of the silver ball with FEM proves quite challenging. Here we can observe some numerical artifacts at the north and south positions of the nano particle. The computation of the scattering field from nano particles provides a challenging benchmark for FEM, as the results can be validated by comparison with the results from the well-established Mie Theory. Therefore further studies of the nano particle are of interest.

#### 6.4 Laser-written waveguide

To test our implementation of hanging nodes for Nédélec elements on non-orientable grids in a practical application in optics simulations, we consider a waveguide created by writing six modifications into a carrier substrate with a laser, causing the substrate to compress in the center. To simulate the behavior of a laser in that waveguide, we use the FEM method, as discussed above again. The geometry is quite complex, so we employ domain decomposition and adaptive mesh refinement. For the simulation, we assume the carrier material to have a refractive index of  $r_{\text{cladding}} = 1.48995$  and the compressed center to have a refractive index of  $r_{\text{center}} = 1.4906$ . The modifications have a distance of 3μm, and the incident laser light has a wavelength of  $\lambda = 660$  nm and is linearly polarised in the  $x$ -direction.

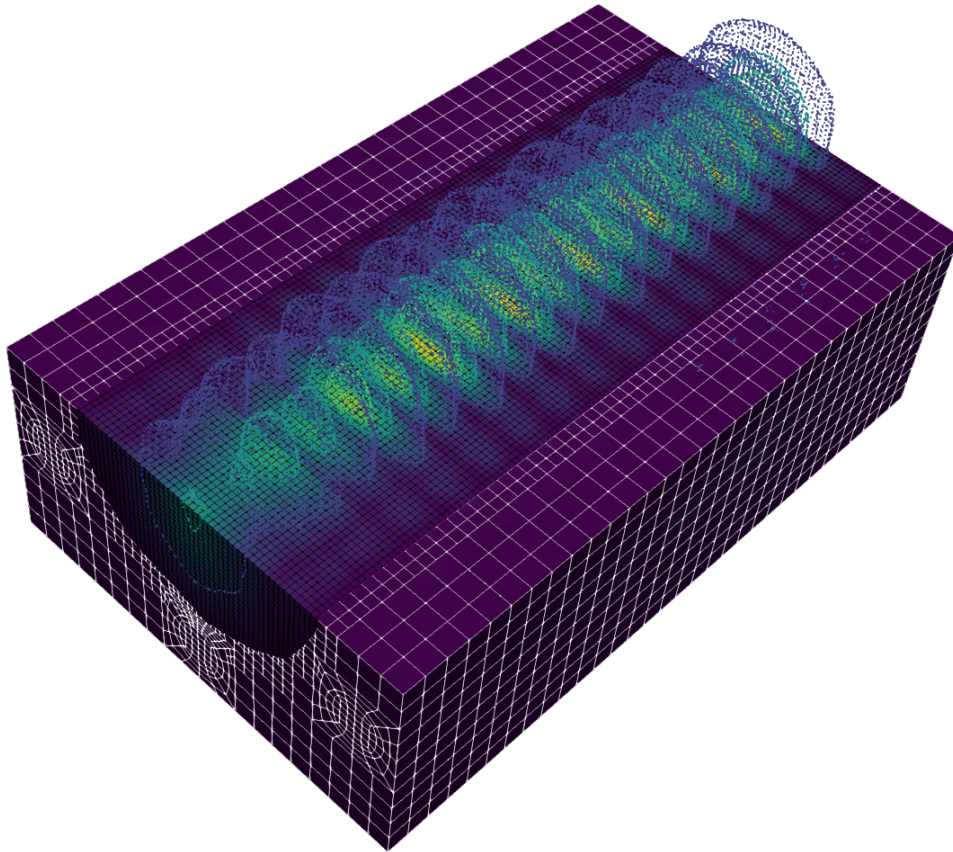


Figure 6.4: Here the electric field’s intensity distribution inside a waveguide is visualized. The black edges represent the edges of the finest level, while the white lines show the edges of the coarser levels.

## 7 Conclusion

In this work, we considered the sign conflict, specifically in scenarios where hanging nodes are present. We provide a comprehensive guide in terms of mathematical derivations and algorithmic designs for resolving this sign conflict. These concepts can be applied to any software package that supports Nédélec elements and locally refined meshes on quadrilaterals or hexahedra with hanging nodes. Our choice is `deal.II` as a programming platform that is highly accessible and user-friendly. The new implementation was demonstrated for four numerical experiments that include qualitative comparisons in two and three spatial dimensions as well as brief computational convergence studies. Finally, a current practical example from optics simulations showing a laser-written wave-guide is presented.

## Acknowledgments

This work is funded by the Deutsche Forschungsgemeinschaft (DFG) under Germany’s Excellence Strategy within the Cluster of Excellence PhoenixD (EXC 2122, Project ID 390833453). Furthermore, we would like to thank Tim Haubold and Philipp König for many fruitful discussions and Clemens Pechstein for tips on how to find mistakes in the implementation.

## References

- [1] Mark Ainsworth and Joe Coyle. 2003. Conditioning of hierarchic  $p$ -version Nédélec elements on meshes of curvilinear quadrilaterals and hexahedra. *SIAM J. Numer. Anal.* 41, 2 (2003), 731–750. <https://doi.org/10.1137/S003614290239590X>
- [2] M. Ainsworth and J. T. Oden. 2000. *A Posteriori Error Estimation in Finite Element Analysis*. Wiley-Interscience [John Wiley & Sons], New York.
- [3] Robert Anderson et al. 2021. MFEM: A Modular Finite Element Methods Library. *Computers & Mathematics with Applications* 81 (2021), 42–74. <https://doi.org/10.1016/j.camwa.2020.06.009>
- [4] Daniel Arndt, Wolfgang Bangerth, Denis Davydov, Timo Heister, Luca Heltai, Martin Kronbichler, Matthias Maier, Jean-Paul Pelteret, Bruno Turcksin, and David Wells. 2020. The deal.II finite element library: Design, features, and insights. *Computers & Mathematics with Applications* (2020). <https://doi.org/10.1016/j.camwa.2020.02.022>
- [5] Daniel Arndt, Wolfgang Bangerth, Marco Feder, Marc Fehling, Rene Gassmüller, Timo Heister, Luca Heltai, Martin Kronbichler, Matthias Maier, Peter Munch, Jean-Paul Pelteret, Simon Sticko, Bruno Turcksin, and David Wells. 2022. The deal.II Library, Version 9.4. *Journal of Numerical Mathematics* 30, 3 (2022), 231–246. <https://doi.org/10.1515/jnma-2022-0054>
- [6] Douglas N. Arnold, Richard S. Falk, and Ragnar Winther. 2000. Multigrid in  $H(\text{div})$  and  $H(\text{curl})$ . *Numer. Math.* 85, 2 (2000), 197–217. <https://doi.org/10.1007/PL00005386>
- [7] I. Babuška and W. C. Rheinboldt. 1978. Error Estimates for Adaptive Finite Element Computations. *SIAM J. Numer. Anal.* 15, 4 (1978), 736–754. <https://doi.org/10.1137/0715049>
- [8] Wolfgang Bangerth and Rolf Rannacher. 2003. *Adaptive Finite Element Methods for Differential Equations*. Birkhäuser, Lectures in Mathematics, ETH Zürich.
- [9] Sven Beuchler, Tim Haubold, and Veronika Pillwein. 2022. Recurrences for Quadrilateral High-Order Finite Elements. *Mathematics in Computer Science* 16, 4 (2022), 32. <https://doi.org/10.1007/s11786-022-00547-2>
- [10] Sven Beuchler, Sebastian Kinnewig, and Thomas Wick. 2022. Parallel Domain Decomposition Solvers for the Time Harmonic Maxwell Equations. In *Domain Decomposition Methods in Science and Engineering XXVI*, Susanne C. Brenner, Eric Chung, Axel Klawonn, Felix Kwok, Jinchao Xu, and Jun Zou (Eds.). Vol. 145. Springer International Publishing, Cham, 653–660. [https://doi.org/10.1007/978-3-030-95025-5\\_71](https://doi.org/10.1007/978-3-030-95025-5_71)
- [11] Craig F. Bohren and Donald R. Huffman. 1998. *Absorption and Scattering of Light by Small Particles* (first ed.). Wiley. <https://doi.org/10.1002/9783527618156>
- [12] M. Bonazzoli, V. Dolean, I. G. Graham, E. A. Spence, and P.-H. Tournier. 2019. Domain decomposition preconditioning for the high-frequency time-harmonic Maxwell equations with absorption. *Math. Comp.* 88, 320 (2019), 2559–2604. <https://doi.org/10.1090/mcom/3447>
- [13] M. El Bouajaji, V. Dolean, M. J. Gander, and S. Lanteri. 2012. Optimized Schwarz Methods for the Time-Harmonic Maxwell Equations with Damping. *SIAM Journal on Scientific Computing* 34, 4 (2012), A2048–A2071. <https://doi.org/10.1137/110842995>

- [14] M. Bürg. 2012. A Residual-Based a Posteriori Error Estimator for the Hp-Finite Element Method for Maxwell’s Equations. *Applied Numerical Mathematics* 62, 8 (Aug. 2012), 922–940. <https://doi.org/10.1016/j.apnum.2012.02.007>
- [15] Leszek Demkowicz. 2007. *Computing with hp-Adaptive Finite Elements*. Chapman & Hall/CRC, Boca Raton.
- [16] Leszek F. Demkowicz, Jason Kurtz, David Pardo, Maciej Paszynski, Waldemar Rachowicz, and Adam Zdunek (Eds.). 2008. *Computing with hp-Adaptive Finite Elements. 2: Frontiers: Three Dimensional Elliptic and Maxwell Problems with Application / Leszek Demkowicz*. Chapman & Hall/CRC, Boca Raton, FL.
- [17] Paolo Di Stolfo, Andreas Schröder, Nils Zander, and Stefan Kollmannsberger. 2016. An Easy Treatment of Hanging Nodes in Hp -Finite Elements. *Finite Elements in Analysis and Design* 121 (2016), 101–117. <https://doi.org/10.1016/j.finel.2016.07.001>
- [18] Clark R. Dohrmann and Olof B. Widlund. 2016. A BDDC algorithm with deluxe scaling for three-dimensional  $H(\mathbf{curl})$  problems. *Comm. Pure Appl. Math.* 69, 4 (2016), 745–770. <https://doi.org/10.1002/cpa.21574>
- [19] K. Eriksson, D. Estep, P. Hansbo, and C. Johnson. 2009. *Computational Differential Equations*. Cambridge University Press.
- [20] O. G. Ernst and M. J. Gander. 2012. Why it is difficult to solve Helmholtz problems with classical iterative methods. In *Numerical analysis of multiscale problems*. Lect. Notes Comput. Sci. Eng., Vol. 83. Springer, Heidelberg, 325–363. [https://doi.org/10.1007/978-3-642-22061-6\\_10](https://doi.org/10.1007/978-3-642-22061-6_10)
- [21] Markus Faustmann, Jens Markus Melenk, and Maryam Parvizi. 2022.  $\mathcal{H}$ -matrix approximability of inverses of FEM matrices for the time-harmonic Maxwell equations. *Adv. Comput. Math.* 48, 5 (2022), Paper No. 59, 32. <https://doi.org/10.1007/s10444-022-09965-z>
- [22] Richard P. Feynman, Robert B. Leighton, and Matthew Sands. 1963. *The Feynman Lectures on Physics. Vol. II. Mainly Electromagnetism and Matter*. California Institute of Technology, Michael A. Gottlieb and Rudolf Pfeiffer.
- [23] Christophe Geuzaine. 2007. GetDP: A General Finite-Element Solver for the de Rham Complex. *PAMM* 7, 1 (2007), 1010603–1010604. <https://doi.org/10.1002/pamm.200700750>
- [24] Alexander V. Grayver and Tzanio V. Kolev. 2015. Large-Scale 3D Geoelectromagnetic Modeling Using Parallel Adaptive High-Order Finite Element Method. *Geophysics* 80, 6 (2015), E277–E291. <https://doi.org/10.1190/geo2015-0013.1>
- [25] F. Hecht. 2012. New Development in FreeFem++. *Journal of Numerical Mathematics* 20, 3-4 (2012), 251–265.
- [26] Stefan Henneking and Leszek Demkowicz. 2022. hp3D User Manual. (2022). <https://doi.org/10.48550/ARXIV.2207.12211> arXiv:arXiv:2207.12211
- [27] Judith Hippold, Arnd Meyer, and Gudula Rünger. 2004. An adaptive, 3-dimensional, hexahedral finite element implementation for distributed memory. In *Computational science—ICCS 2004. Part II*. Lecture Notes in Comput. Sci., Vol. 3037. Springer, Berlin, 146–154. [https://doi.org/10.1007/978-3-540-24687-9\\_19](https://doi.org/10.1007/978-3-540-24687-9_19)
- [28] R. Hiptmair. 1999. Multigrid method for Maxwell’s equations. *SIAM J. Numer. Anal.* 36, 1 (1999), 204–225. <https://doi.org/10.1137/S0036142997326203>

- [29] Janne Keranen, Jenni Pippuri, Mika Malinen, Juha Ruokolainen, Peter Raback, Mikko Lyly, and Kari Tammi. 2015. Efficient Parallel 3-D Computation of Electrical Machines With Elmer. *IEEE Transactions on Magnetics* 51, 3 (March 2015), 1–4. <https://doi.org/10.1109/TMAG.2014.2356256>
- [30] Tobias Knoke, Sebastian Kinnewig, Sven Beuchler, Ayhan Demircan, Uwe Morgner, and Thomas Wick. 2023. Domain Decomposition with Neural Network Interface Approximations for Time-Harmonic Maxwell’s Equations with Different Wave Numbers. *Selecciones Matemáticas* (2023). <https://doi.org/10.17268/se1.mat.2023.01.01>
- [31] Pavel Kus, Pavel Solin, and David Andrs. 2014. Arbitrary-Level Hanging Nodes for Adaptive hp-FEM Approximations in 3D. *J. Comput. Appl. Math.* 270 (2014), 121–133. <https://doi.org/10.1016/j.cam.2014.02.010>
- [32] R.M. Kynch and P.D. Ledger. 2017. Resolving the Sign Conflict Problem for Hp–Hexahedral Nédélec Elements with Application to Eddy Current Problems. *Computers & Structures* 181 (2017), 41–54. <https://doi.org/10.1016/j.compstruc.2016.05.021>
- [33] Konstantin Ladutenko, Ovidio Peña Rodríguez, Paul Müller, and The Gitter Badger. 2017, <https://doi.org/10.5281/zenodo.248729>. ovidiop/scattnlay: The second stable release. <https://doi.org/10.5281/zenodo.248729>
- [34] Nicolas Lebbe. 2016. *Contribution in Topological Optimization and Application to Nanophotonics*. Ph. D. Dissertation. University Grenoble Alpes.
- [35] Hatam Mahmudlu, Robert Johanning, Albert Van Rees, Anahita Khodadad Kashi, Jörn P. Epping, Raktim Halder, Klaus-J. Boller, and Michael Kues. 2023. Fully On-Chip Photonic Turnkey Quantum Source for Entangled Qubit/Qudit State Generation. *Nature Photonics* (2023). <https://doi.org/10.1038/s41566-023-01193-1>
- [36] O. Melchert, S. Kinnewig, F. Dencker, D. Perevoznic, S. Willms, I. Babushkin, M. Wurz, M. Kues, S. Beuchler, T. Wick, U. Morgner, and A. Demircan. 2023. Soliton Compression and Supercontinuum Spectra in Nonlinear Diamond Photonics. *Diamond and Related Materials* 136 (2023), 109939. <https://doi.org/10.1016/j.diamond.2023.109939>
- [37] Peter Monk. 2003. *Finite Element Methods for Maxwell’s Equations*. Clarendon Press ; Oxford University Press, Oxford : New York.
- [38] J. C. Nédélec. 1980. Mixed Finite Elements in  $\mathbb{R}^3$ . *Numer. Math.* 35, 3 (1980), 315–341.
- [39] Jean-Claude Nédélec. 1986. A New Family of Mixed Finite Elements in  $\mathbb{R}^3$ . *Numer. Math.* 50 (1986), 57–81.
- [40] Maryam Parvizi, Amirreza Khodadadian, Sven Beuchler, and Thomas Wick. 2023. Hierarchical LU Preconditioning for the Time-Harmonic Maxwell Equations. In *Domain decomposition methods in science and engineering XXVII*. Springer, Heidelberg. <https://doi.org/10.48550/arXiv.2211.11303> accepted for publication.
- [41] S. Repin. 2008. *A Posteriori Estimates for Partial Differential Equations*. Radon Series on Computational and Applied Mathematics, Vol. 4. Walter de Gruyter GmbH & Co. KG, Berlin. xii+316 pages.
- [42] Joachim Schöberl. 1997. NETGEN An Advancing Front 2D/3D-mesh Generator Based on Abstract Rules. *Computing and Visualization in Science* 1, 1 (July 1997), 41–52. <https://doi.org/10.1007/s007910050004>
- [43] Joachim Schöberl et al. [n.d.]. GitHub - NGSolve/NGsolve: Netgen/NGSolve Is a High Performance Multiphysics Finite Element Software. <https://github.com/NGSolve/ngsolve>.

- [44] Matthew W. Scroggs, Jørgen S. Dokken, Chris N. Richardson, and Garth N. Wells. 2022. Construction of Arbitrary Order Finite Element Degree-of-Freedom Maps on Polygonal and Polyhedral Cell Meshes. *ACM Trans. Math. Software* 48, 2 (2022), 1–23. <https://doi.org/10.1145/3524456>
- [45] B. A. Szabo and Ivo Babuška. 2021. *Finite Element Analysis: Method, Verification and Validation* (second edition ed.). Wiley, Hoboken, NJ.
- [46] Gábor Szegő. 1939. *Orthogonal Polynomials* (4th ed ed.). Number v. 23 in Colloquium Publications - American Mathematical Society. American Mathematical Society, Providence.
- [47] B. Thierry, A. Vion, S. Tournier, M. El Bouajaji, D. Colignon, N. Marsic, X. Antoine, and C. Geuzaine. 2016. GetDDM: An Open Framework for Testing Optimized Schwarz Methods for Time-Harmonic Wave Problems. *Computer Physics Communications* 203 (2016), 309–330. <https://doi.org/10.1016/j.cpc.2016.02.030>
- [48] Andrea Toselli. 2006. Dual-primal FETI algorithms for edge finite-element approximations in 3D. *IMA J. Numer. Anal.* 26, 1 (2006), 96–130. <https://doi.org/10.1093/imanum/dri023>
- [49] R. Verfürth. 1996. *A Review of A Posteriori Error Estimation and Adaptive Mesh-Refinement Techniques*. Wiley/Teubner, New York-Stuttgart.
- [50] Sabine Zaglmayr. 2006. *High Order Finite Element Methods for Electromagnetic Field Computation*. Ph.D. Dissertation. Johannes Kepler University Linz.
- [51] O.C. Zienkiewicz and J.Z. Zhu. 1992. The Superconvergent Patch Recovery and a Posteriori Error Estimates. Part 2: Error Estimates and Adaptivity. *Int. J. of Numer. Methods Engrg.* 33, 7 (1992), 1365–1382.
- [52] M. Zolgharni, P. D. Ledger, and H. Griffiths. 2009. Forward Modelling of Magnetic Induction Tomography: A Sensitivity Study for Detecting Haemorrhagic Cerebral Stroke. *Medical & Biological Engineering & Computing* 47, 12 (2009), 1301–1313. <https://doi.org/10.1007/s11517-009-0541-1>